### Title

Facet-selective etching trajectories of individual semiconductor nanocrystals




### Journal

Science Advances, 8(32)

### ISSN

2375-2548



### Authors

Yan, Chang

Byrne, Dana

Ondry, Justin C

et al.



### Publication Date

2022-08-12

### DOI

10.1126/sciadv.abq1700

Peer reviewed

# Title: Facet-Selective Etching Trajectories of Individual Semiconductor Nanocrystals

**Short title:** Electron microscopy tracks etching of quantum dots

**Authors:** Chang Yan[1,2], Dana Byrne[1], Justin C. Ondry[1,3], Axel Kahnt[4], Ivan A. Moreno-Hernandez[1], Gaurav A. Kamat[5], Zi-Jie Liu[1], Christian Laube[1,4], Michelle F. Crook[1], Ye Zhang[1], Peter Ercius[6], and A. Paul Alivisatos[1,2,3,7]*†

**Affiliations:**

[1]Department of Chemistry, University of California, Berkeley; Berkeley, California 94720, United States.

[2]Materials Sciences Division, Lawrence Berkeley National Laboratory; Berkeley, California 94720, United States.

[3]Kavli Energy NanoScience Institute, University of California, Berkeley; Berkeley, California 94720, United States.

[4]Leibniz Institute of Surface Engineering (IOM); Permoserstr. 15, D-04318 Leipzig, Germany.

[5]Department of Chemical and Biomolecular Engineering, University of California, Berkeley; Berkeley, California 94720, United States.

[6]National Center for Electron Microscopy, Molecular Foundry, Lawrence Berkeley National Laboratory; Berkeley, California 94720, United States.

[7]Department of Materials Science and Engineering, University of California, Berkeley; Berkeley, California 94720, United States.

*Corresponding author. Email: paul.alivisatos@uchicago.edu

†Current address: Department of Chemistry, The University of Chicago; Chicago, IL, 60637

**Abstract:** The size and shape of semiconductor nanocrystals govern their optical and electronic properties. Liquid cell transmission electron microscopy (LCTEM) is an emerging tool that can directly visualize nanoscale chemical transformations, and therefore inform the precise synthesis of nanostructures with desired functions. However, it remains difficult to controllably investigate the reactions of semiconductor nanocrystals with LCTEM, due to the highly reactive environment formed by radiolysis of liquid. Herein, we harness the radiolysis processes, and report the single-particle etching trajectories of prototypical semiconductor nanomaterials with well-defined crystalline facets. PbSe nanocubes represent an isotropic structure which retains the cubic shape during etching via a layer-by-layer mechanism. The anisotropic arrow-shaped CdSe nanorods possess polar facets terminated by either Cd or Se atoms, and the transformation trajectory is driven by etching the Se-terminated facets. LCTEM trajectories reveal how nanoscale shape transformations of semiconductors are governed by the reactivity of specific facets in liquid environments.

**Teaser:** Single-particle reaction pathways of semiconductor nanocrystals in liquid are directly visualized by electron microscopy.

## MAIN TEXT

### Introduction

Semiconductor nanocrystals possess widely tunable optical and electrical properties which depend critically on their size and shape (*1–3*). This feature has enabled a diverse array of opportunities and applications such as biological imaging (*4*), luminescent solar concentrators (*5*), quantum dot lasers (*6*) and displays (*7*, *8*). Tuning the properties of semiconductor nanocrystals relies on the ability to precisely control their size and shape evolution during growth and etching processes. The reactivity of specific bulk crystal facets towards growth and etching reactions have been systematically characterized, enabling the fabrication of almost arbitrary patterns in top-down bulk semiconductor processing (*9*). In contrast, it is challenging to directly investigate the reaction mechanisms of nanocrystals since multiple facets are in close proximity, and the large fraction of edge sites and facet intersections lead to complex interactions that are difficult to predict (*10*). Furthermore, the thermodynamics of colloidal nanocrystals, as well as the kinetics of their growth and dissolution, are far richer than those of bulk crystals, due to the influence of the organic-inorganic interfaces that help to define them (*11*, *12*). *In-situ* tools with nanoscale spatial resolution, which can operate in the reactive liquid environments used to process structures, are needed to visualize and ultimately understand pertinent transformations.

Liquid cell transmission electron microscopy (LCTEM) has demonstrated the necessary spatial and temporal resolution for observation of nanoscale dynamics, including self-assembly processes (*13*), diffusion and rotation motions (*14*), growth reactions (*15*, *16*), and etching reactions (*17*). However, LCTEM studies have mostly been limited to noble metal nanocrystals due to the inability to precisely control the chemical environment formed by radiolysis, which can cause reactive materials such as metal chalcogenide semiconductors to degrade uncontrollably. Recent studies in understanding and regulating the radiolytic redox environment in LCTEM (*18–21*) suggest that it may now be possible to design new LCTEM environments specifically for controlled observations of single-particle etching trajectories of reactive nanocrystals. While previous studies on the etching of noble metal nanocrystals were performed with highly acidic solutions containing inorganic metal halides (*17–19*, *21*), herein we utilize tris(hydroxymethyl)aminomethane hydrochloride (Tris·HCl), an organic molecule, as the only additive in water which results in a much milder steady-state pH and redox environment essential for the controlled etching of sensitive semiconductor nanocrystals. Tris·HCl dissociates into $TrisH^+$ cation and $Cl^-$ anion in water, and forms a weakly acidic solution with pH = 3~5 under electron beam irradiation. The $TrisH^+$ cation, as will be shown here, can act to set the etching electrochemical potential in the liquid cell. Two types of technologically important prototype semiconductor nanocrystals are chosen for the investigation: lead selenide (PbSe) with a higher symmetry isotropic rocksalt lattice, and cadmium selenide (CdSe) with a lower symmetry anisotropic wurtzite lattice. The high degree of synthesis control over the size and shape of these nanocrystals enables us to systematically examine nanoscale surface phenomena such as the relative reactivity and stability of different crystal facets over a wide range of etching kinetics.

As depicted in Fig. 1, an aqueous pocket containing the nanocrystals is sandwiched between the ultrathin carbon layers of two TEM grids. The aqueous layer has a thickness of tens of nanometers and each carbon layer has a thickness of a few nanometers. These layers are sufficiently thin to reduce electron scattering to the level that allows high-resolution images to be formed. Radiolysis reactions are triggered by beam-sample interactions within the aqueous layer (*19*, *22*, *23*), forming a mixture of non-equilibrium redox-active species such as hydroxyl radicals, atomic hydrogen, and solvated electrons (*22*). Hydroxyl radical is a highly oxidative species with a standard electrode potential of 1.9 V vs the normal hydrogen electrode (*24*). Experimental

evidence, along with kinetic modeling, indicates that the $TrisH^+$ cation reacts rapidly with the hydroxyl radical via a hydrogen abstraction reaction to consume the hydroxyl radical and form an amine radical cation $Tris^{\bullet+}$ (supplementary text, and fig. S1-S7). The standard electrode potentials of amine radical cations are in the range of 0.8~1.3 V, suitable for etching metal chalcogenides (*25–27*). Thus, the Tris·HCl additive regulates the electrochemical potential of etching process. Kinetic modeling results (fig. S5-S6) were included in the supplementary materials to calculate the estimated concentration and electrochemical potential of the amine radical species in the liquid cell.

## Results

### Layer-by-layer etching of PbSe nanocrystals

A representative TEM image of a PbSe nanocube in vacuum is shown on Fig. 2A, indicating that the nanocube is terminated by {100} facets on the six faces of the cube (fig. S8). {111} and {110} facets can be exposed by truncating the corners and the edges of the cube, respectively (Fig. 2B). The square-shaped image of an intact cube in Fig. 2A is a projection along the [100] zone axis and exhibits the regular spacing of 0.309 nm, as measured by Fourier analysis of the image, that corresponds to {200} planes of PbSe (*28*, *29*). In the liquid pocket, this characteristic {200} *d*-spacing is observed during the etching process, indicating that the unetched portion of the particle remains as PbSe (Fig. 2C). The orientation of the {200} planes, and therefore the orientation of the nanocrystal does not change throughout the etching process (fig. S9-S11) even after the particle becomes truncated.

A time-series of LCTEM images in Fig. 2D illustrate the etching trajectory of a PbSe nanocrystal at an applied electron fluence rate of 400 $e^{-}\cdot Å^{-2}\cdot s^{-1}$ (movie S1). As the etching begins, the edges and corners etch slightly, leading to minor truncation. Instead of undergoing further etching of the {111} and {110} facets, the PbSe nanocrystal largely retains the cubic shape with {100} termination as the etching progresses. In Fig. 2F, the outlines of PbSe nanocrystal extracted from LCTEM images are displayed at equal time intervals. The majority of the outlines are rounded squares except for a few outlines captured towards the end of etching trajectory.

The persistence of the cubic shape indicates that atoms from the nanocrystal are removed via a layer-by-layer etching mechanism. The layer-by-layer mechanism can be explicated by the Terrace-Step-Kink (TSK) model which describes solid surface reactivity (*30*, *31*). In the PbSe lattice, each Pb or Se atom has six nearest Se or Pb neighbors arranged in an octahedral coordination environment. The coordination number of six is reduced to five, four and three for surface atoms on {100}, {110} and {111} facets, respectively. The surface atoms with higher numbers of missing bonds are thus easier to remove, causing the truncation of corners and edges at the initial stage of etching. This truncation also forms a terrace layer of atoms on top of pristine facets. In the TSK model of a simple cubic lattice, a terrace contains under-coordinated sites such as adatoms, vacancies, kink and step atoms, of which the coordination numbers are less than four. As etching occurs, these under-coordinated sites continue to develop within or on the edges of terraces, rendering a terrace more reactive than a pristine facet, and the terraces are removed rapidly upon formation. The process during which a terrace on {100} facets are formed and then selectively removed is illustrated in Fig. 2H. The trajectory in Fig. 2F indicates that the removal of terrace layers on any exposed facets, mainly the {100} facets, competes favorably with further truncations on intact {110} or {111} facets. The terrace layers are completely etched away before the etching of atoms in the next pristine layer occurs, retaining the cubic shape of the nanocrystal with {100} termination.

The layer-by-layer etching mechanism in the liquid environment here is consistent with the previously observed sublimation pathways of PbSe nanocrystals at elevated temperatures

under high vacuum (*32*). In both cases, the trajectories cannot be explained by only considering the higher reactivity of {111} and {110} facets over {100} facets. Otherwise, the relative areas of the higher index facets on the corners and edges would increase during etching, and turn the cubic shape into polygons. The TSK model, which introduces highly reactive incomplete terraces, implies that the etching condition here forms many under-coordinated sites which could be considered as reactive 'defects' on the surface of the nanocrystal. If milder etching conditions were applied, for instance by replacing $Tris^{\bullet+}$ with a less oxidizing radical species, it would be possible to suppress the formation of the 'defects' and selectively etch the {111} facets.

Towards the end of the etching trajectory, the curvature of the nanocrystal surface increases and the area of {100} facets become comparable to the area of other high index facets. The layer-by-layer mechanism becomes less dominant at this stage, and etching appears to occur more homogeneously in all directions. The outlines in Fig. 2F turn into polygons, and eventually circular shapes with more uniform curvatures as the nanocrystal size is reduced to only a few nanometers.

A loss of facet selectivity is observed when a high electron fluence was applied to etch the PbSe nanocrystals. Fig. 2E displays the time-lapse LCTEM images of a PbSe nanocrystal etched at 2000 $e^{-}\cdot Å^{-2}\cdot s^{-1}$ which finishes within 5 seconds (movie S2). This is ~10 times shorter than that at 400 $e^{-}\cdot Å^{-2}\cdot s^{-1}$ (Fig. 2I). Fig. 2I displays the average etching kinetics of several nanocrystals, and the kinetics for individual nanocrystals are summarized in fig. S12. The intermediate shapes of the PbSe nanocrystal in Fig. 2E deviate significantly from a regular cubic shape as compared to those in Fig. 2D. In Fig. 2G, the outlines extracted from LCTEM images recorded at 2000 $e^{-}\cdot Å^{-2}\cdot s^{-1}$ also appear to be more irregular than the outlines shown in Fig. 2F. In the fast etching scenario, the trajectory suggests that the etching of the next atom layer has begun before the terrace layer is fully removed. Consistent with the observation that regulating growth rate is critical for synthesizing nanocrystals with well-defined facets (*33*, *34*), the results here indicate that etching selectivity also critically depends on the reaction rate.

Previously we reported that the selectivity of etching certain facets on gold nanocrystals can be tuned by varying the chemical potential and the concentration of additive such as $FeCl_3$ in liquid cells (*17*, *21*). For gold nanocrystals, the electron fluence rate acts as a finer control over the etching trajectories than the concentration of $FeCl_3$. At the same electron fluence rate, etching trajectories recorded with lower concentrations of $FeCl_3$ exhibit higher selectivity than those recorded with higher concentrations of $FeCl_3$. At the same concentration of $FeCl_3$, varying the electron fluence rate in the range of 200-1200 $e^{-}\cdot Å^{-2}\cdot s^{-1}$ affects the etching rate but not the facet selectivity. Herein, in comparison, the facet selectivity of etching semiconductor nanocrystals is sensitive to the electron fluence rate. Semiconductor materials such as PbSe and CdSe are generally much more prone to oxidative etching than noble metals such as gold. It is possible that the fast etching at 2000 $e^{-}\cdot Å^{-2}\cdot s^{-1}$ generates enough number of surface defects that significantly reduces the differences in the reactivity of various facets and terraces. Furthermore, it had been proposed that the surface diffusion of gold atoms can passivate defect sites generated during etching (*17*, *35*), but such diffusion processes may have larger kinetic barriers, especially for selenide anions (*36*), for the semiconductor nanocrystals investigated here.

LCTEM imaging captures the formation of a substance with lighter image contrast around the PbSe nanocrystals as a product of the etching reactions. Further analysis reveals that the *d*-spacings identified for the product match the values of $PbCl_2$ (fig. S13). These results suggest that during the etching process selenium is oxidized and dispersed into the liquid, and lead forms $PbCl_2$ precipitates with chloride ions in the pocket.

**Anisotropic etching of CdSe nanocrystals**

In contrast to the cubic lattice of PbSe, wurtzite CdSe features an anisotropic lattice which can be considered as alternating layers of Cd and Se atoms along the $[0001]$ axis (*c*-axis). During the growth of wurtzite CdSe nanocrystals, it is suggested that surfactant ligands bind favorably to the Cd-terminated facets, causing the Se-terminated facets to grow faster (*37*, *38*). The resulting nanocrystal is therefore elongated into a nanorod of which the Se-terminated end appears as arrow-shaped due to faster growth (fig. S14). In Fig. 3A, we present the structure of a CdSe nanorod resolved by aberration-corrected high-angle annular dark-field scanning transmission electron microscopy (AC-HAADF-STEM) in vacuum. HAADF-STEM images are formed by collecting electrons scattered to high angles by atoms in the material, leading to mass-thickness image contrast, which scales approximately as $Z^2$, where Z is the atomic number. Therefore, Cd will be brighter compared to Se. The enlarged inset in Fig. 3A clearly shows that the nanocrystal consists of alternating layers of brighter (Cd) and dimmer (Se) atomic columns. We label Cd with pink solid circles and Se with green solid circles on top of the image to guide visualization. The HAADF-STEM image shows the orientation of the alternating atomic layers: the termination facet on the tip of the 'arrow' is a layer of Se atoms and the opposite termination facet on the flat side is a layer of Cd atoms (fig. S15-S22). This establishes the relationship between nanoscale morphology and the polar arrangement of Cd and Se atoms (atomic scale polarity) in the lattice.

The contrast of HAADF-STEM images decreases significantly for the terminal layers at the edges (fig. S18, S21-S22). The lower HAADF intensity indicates that the terminal layer is a terrace or a partial layer rather than a full layer. Therefore, the analysis has been focused on the clearly interpretable full layers. Careful inspection of the STEM images indicates the polarity seen in the previous layers continues into the terminal layer. It is expected that the terminal layer has the same polarity as the full layers for the following reasons. Each Cd or Se atom has four nearest Se or Cd neighbors arranged in a tetrahedral coordination environment. An atom within each layer of atomic columns, as shown in Fig. 3A, forms one bond to an atom in the adjacent layer and three bonds to three atoms in the other adjacent layer arranged in the opposite direction. Exposure of an atomic layer where the atoms miss three bonds forms a highly unstable facet that will be passivated or removed by adding or subtracting another atomic layer during growth or etching processes so that the atomic scale polarity along the *c*-axis is preserved throughout the nanorod.

The nanoscale morphology (shape) of the nanorod can be analyzed from a line profile of pixel intensities along the short axis. As shown in the lower right panel of Fig. 3A, the intensity of the HAADF-STEM image peaks at the center of the rod and gradually reduces towards the edge of the rod, consistent with the expected hexagonal cross section of the rod. The center of the rod is the location of a hexagonal vertex, and this thicker region scatters more electrons. By imaging a nanorod sitting on the *c*-axis, the hexagonal projection of the nanorod can be easily observed from the bright field TEM image in Fig. 3B. Crystal lattices with hexagonal structures such as wurtzite can be described conveniently by the four-axis Miller-Bravais index system (materials and methods) (*39*). The Se-terminated tip of the nanorod corresponds to the $(000\bar{1})$ basal facet, the Cd-terminated bottom corresponds to the $(0001)$ basal facet, and the six hexagonal sides of the nanorod correspond to the $\{\bar{1}100\}$ family of prismatic facets.

The reactivity of a specific facet in a CdSe nanorod depends critically on the composition of the facet. Fig. 3C illustrates the atomistic model of a nanorod which has the same projection direction as the HAADF-STEM image. Besides the $(000\bar{1})$ facet on the tip, the two facets that correspond to the two corners near the Cd-terminated bottom of the rod, $(\bar{1}101)$ and $(1\bar{1}01)$ facets, are also terminated with Se (fig. S17-S18). In Fig. 3A, we can observe that the Se-terminated corners, $\{1\bar{1}01\}$ facets, and the $(000\bar{1})$ tip have smaller areas compared to the areas of prismatic

facets and the Cd-terminated facets: $\{1\bar{1}01\}$ and $(0001)$ facets. During the growth of the nanorods, the area of the more reactive Se-terminated facets shrinks while the areas of more stable facets increase due to higher growth rate on the Se-terminated facets. On the contrary, etching processes are expected to enlarge the areas of unstable Se-terminated facets as the Se atoms are prone to oxidation by the radicals generated by radiolysis. The polar terminations of the facets are further illustrated by 3D models in fig. S15.

The time-lapse LCTEM images of a CdSe rod etched at 400 $e^{-}\cdot Å^{-2}\cdot s^{-1}$ are shown in Fig. 3D (movie S3). The regular (0002) spacing of 0.350 nm can be resolved in the LCTEM images by Fourier analysis (Fig. 3F), demonstrating the samples remain as pristine CdSe before and during etching. As the etching proceeds, the orientation of the $\{0002\}$ planes does not change and the rod does not rotate (fig. S23-S24). Within the first five seconds, the sharp tip of the rod flattens while the bottom of the rod etches from the two corners. The selective etching of the three Se-terminated facets, as illustrated in Fig. 3C, inverts the 'arrow' direction of the nanorod. An example of the inverted arrow-shaped intermediate is captured at $t$ = 4.25 s in Fig. 3D. The inversion process is also demonstrated by the evolution of the outlines plotted with an equal time gap in Fig. 3G. Consistent with *in-situ* TEM observations on the sublimation of CdSe nanorods (*31*), we find that etching occurs faster along the long axis of the rod than along the short axis, due to the higher stability of prismatic facets. The anisotropic etching eventually transforms the rod to a circular object near the end of the trajectory. Analysis of the *d*-spacings from the spatial Fourier transform patterns indicates that the most plausible etching product of CdSe is $CdCl_2{\bullet}HCl{\bullet}H_2O$ (fig. S25).

We note that the anisotropic etching of the CdSe nanorod driven by the selective etching of Se-terminated facets is favored under moderate etching conditions. As shown by the time-lapse LCTEM images in Fig. 3E, a nanorod etched at 2000 $e^{-}\cdot Å^{-2}\cdot s^{-1}$ largely retains the initial arrow shape until the end of the trajectory (movie S4), similar to the layer-by-layer etching trajectory of PbSe discussed above. The persistence of the initial shape is also manifested by the outline evolution in Fig. 3H. At the fluence rate of 2000 $e^{-}\cdot Å^{-2}\cdot s^{-1}$, etching finishes in ~4 seconds on average, while the average duration of the etching trajectories at 400 $e^{-}\cdot Å^{-2}\cdot s^{-1}$ is ~20 seconds (Fig. 3I, fig. S26). When the etching rate is sufficiently high, it is possible that defect sites such as those discussed above for the TSK model of PbSe nanocrystals become significant on various terminal facets of the CdSe nanorods. The generation of surface defects can render the differences of dissolution rates among surface facets smaller than the differences among pristine wurtzite facets. If the electron fluence rate could be set even higher or stronger oxidizing species were present, we can expect etching to occur rapidly on all of the facets, including the more stable prismatic facets.

We also performed *in-situ* etching experiments on arrow-shaped CdSe nanorods of which the prismatic faces are $\{11\bar{2}0\}$ facets (*40*, *41*) (movies S5-S6). These nanorods have the same facet polarity along the *c*-axis as the nanorods with $\{\bar{1}100\}$ prismatic facets, except for the hexagonal prismatic faces are rotated by 90° around the long *c*-axis of the rod (fig. S19-S21). For the $\{11\bar{2}0\}$ nanorods, we report the same etching patterns as those of the $\{\bar{1}100\}$ nanorods discussed above (fig. S27-S28). This observation shows that the facet-selective etching mechanism is dominated by the *c*-axis polarity, rather than the prismatic facet termination.

The majority of the CdSe nanorods studied thus far are projected along the short axis instead of the long axis due to their high aspect-ratio. To examine the shape evolution projected along the *c*-axis of the wurtzite CdSe nanocrystals, we synthesized disk-like CdSe nanocrystals where the width across the prismatic facets is comparable to the length along the *c*-axis (fig. S29). The nanocrystals mostly exhibit a hexagonal projection along the *c*-axis (Fig. 4A). The Se-

terminated $(000\bar{1})$ facet on the tip points towards the viewer as illustrated by the atomistic model in Fig. 4B.

Upon etching at the applied fluence rate of 400 $e^{-}\cdot Å^{-2}\cdot s^{-1}$, we observe that the center of the hexagon has lighter contrast compared to the outer regions (Fig. 4A and fig. S30, movie S7). In Fig. 4C, we examine the temporal evolution of the transmitted electron fluence rates detected in different image segments. The camera used for LCTEM imaging has been calibrated so that we can directly relate camera counts to counts of incident electrons per pixel in a unit time (Materials and Methods). Thus, the grayscale value registered at each pixel of a TEM image is converted to the detected electron fluence rate at the pixel, quantifying the electron counts per unit area in a unit time on the camera. The background fluence rate of liquid averaged over the area outside of the nanocrystal does not vary much during the etching. Data in Fig. 4C show that the etching of CdSe gradually brings the fluence rates detected in the region occupied by the nanocrystal towards the background fluence rate. The increment of detected electron fluence rate in an image segment indicates that the nanocrystal is becoming thinner in the region, since thicker materials scatter more electrons. The etching proceeds faster within the segmented regions closer to the center of the hexagon, suggesting the formation of a concave pit similar to the wet etching of silicon wafers (*9*), as illustrated in Fig. 4D. The results corroborate the conclusion that the etching of the Se-terminated $(000\bar{1})$ facet of wurtzite CdSe nanocrystals is highly favored over the etching of the more stable prismatic facets.

We previously reported that the etching trajectories of gold nanorods could be analyzed using the local curvatures of object outlines measured from LCTEM images (*17*). While high curvature features generally correspond to high index facets which are more reactive, the semiconductor etching trajectories reported here cannot be simply attributed to local curvatures. For instance, the vertices of the hexagonal projection in Fig. 4A have high local curvatures, but etching over the prismatic facets barely occurs. Factors such as the concurrence of cations and anions in the lattice, and the polar facets in the anisotropic wurtzite lattice, do not apply for the case of gold nanocrystals.

## Discussion

The surface energy and facet-dependent reactivity of important bulk semiconductors such as silicon and group III-V semiconductors (*42*, *43*) have been carefully examined under different conditions. With the aid of LCTEM, we demonstrate that it is possible to directly examine the facet-dependent reactivity of colloidal semiconductor crystals on the nanoscale. The microscopic trajectories have confirmed the relative reactivity of different facets of semiconductor nanocrystals learned from copious practice of nanocrystal synthesis. Moreover, as we reverse the direction of transformation, the selective etching can generate transformation pathways, shapes, and functions different from these obtained from growth reactions. In contrast to the classical methods of sampling reaction intermediates such as taking aliquots, we highlight the capacity of LCTEM to provide real-time, continuous structural trajectories.

One aspect we have not discussed is the possible effect of ligands on the etching trajectories. Studies have shown that the presence or removal of ligands can impact self-assembly and etching of nanocrystals in LCTEM experiments (*20*, *44*). Though the etching mechanisms we proposed here do not invoke the participation of ligands, it is plausible for ligands such as oleic acid or chloride ions to dynamically bind to the surface of nanocrystals as etching occurs. The effect of ligands could be assessed by etching nanocrystals stripped of native ligands or covered with various types of ligands in future works.

It is remarkable that sensitive nanomaterials such as PbSe can be investigated controllably with LCTEM. The approach of using an organic additive such as Tris·HCl to regulate the

radiolytic redox environment in liquid cell electron microscopy may also be more broadly applied to studies involving fragile species such as biological macromolecules. Furthermore, the buffer capacity of Tris·HCl/Tris conjugate acid-base pair could be explored to regulate the pH in liquid cells. For future studies, LCTEM holds the potential to provide real-time information on the transformation of an array of functional nanostructures with increasing complexity, such as core/shell nanocrystals and nanocrystals assembled via inorganic-organic interfaces.

## Materials and Methods

### Notations of crystallography

For PbSe nanocrystals, we use the Miller indices based on three orthogonal vectors to describe crystal axes and planes. Square brackets describe the crystal axes and parentheses describe the crystal planes, e.g. [100] axis and (100) plane. Families of crystal axes and families of crystal planes which are related by symmetry are denoted by angled brackets and curly brackets, respectively (e.g. $\langle 100 \rangle$ axes and {100} planes).

For wurtzite CdSe nanocrystals with hexagonal structures, we use the Miller-Bravais indices based on four vectors to describe crystal axes and planes, *e.g.* $[\acute{1}\,100]$axis and $(\acute{1}\,100)$ plane (*39*). The first three numbers from left to right correspond to three in-plane directions each separated by 120°, and the fourth number corresponds to the direction perpendicular to the plane formed by the other three vectors (fig. S15-S16). $[000\,\acute{1}]$ represents the axis pointing to the opposite direction of [0001] axis. Families of crystal axes and families of planes which are related by symmetry are denoted by angled brackets and curly brackets, respectively (*e.g.* $\langle \acute{1}\,100 \rangle$ axes and $\{\acute{1}\,100\}$ planes).

### Materials

Cadmium oxide (CdO, 99.99%, Aldrich), lead oxide (PbO, 99.999%, Aldrich), selenium (Se, 99.99%, powder, Aldrich), oleic acid (OA, 90%, technical grade, Aldrich), oleylamine (OAm, technical grade 70%, Aldrich), octadecene (ODE, 90%, technical grade, Aldrich), *n*-trioctylphosphine (TOP, 97%, Strem Chemicals), cetyltrimethylammonium chloride (CTAC, >95%, TCI), dioctyl ether (OE, 99%, Aldrich), dibenzyl ether (98%, Aldrich)

### Synthesis and characterization of PbSe and CdSe nanocrystals

PbSe nanocubes were synthesized using published protocols (*29*). CdSe nanorods were synthesized based on variations of our published methods (*40*).

*Synthesis of PbSe nanocubes (Fig. 2, fig. S9-S12).* 0.40 mmol of PbO (89 mg), 4 mL of OA, 2 mL of OAm, and 14 mL of dry ODE were loaded into a 50 mL three-neck round-bottom flask and degassed on a Schlenk line at 110 °C for 30 minutes. Then the Schlenk line was switched back to argon, and the flask was heated to 210 °C for 20 minutes. The mixture turned transparent. Meanwhile, 0.49 mmol of Se (39 mg) and 5 mL of dry ODE were loaded into a 25 mL three-neck round-bottom flask and heated under argon on a Schlenk line at 200 °C for 30 minutes until all the Se dissolved, forming a 0.1 M Se solution in ODE. Then the solution was cooled down to room temperature under argon, and 2 mL of the solution was extracted by a syringe. The contents of the syringe were rapidly injected into the Pb complex solution at 210 °C and the reaction was allowed to proceed for 6.5 min under argon. The black-colored samples were cooled to room temperature and transferred to an argon-filled glove box for cleaning. First, 20 mL of anhydrous isopropanol and 5 mL of anhydrous methanol were added as the non-solvent, and the nanocrystals were precipitated by centrifugation at 11000 rpm. The resulting pellet was dissolved in hexanes. The particles were further precipitated twice at 8000 rpm using isopropanol/ hexanes as the non-solvent/solvent pair. The PbSe nanocubes, 18~25 nm in size, were dissolved

in hexanes and stored in an argon glove box. The static TEM and XRD characterization are shown in fig. S8.

*Synthesis of CdSe seeds.* 8 mmol of CdO (1028 mg), 20 mmol of OA (6.4 mL), and 40 mL of ODE were loaded into a 100 mL three-neck round-bottom flask and degassed on a Schlenk line at 110 °C for 1 h. The flask was filled with argon and heated to 210 °C to form a Cd-oleate complex. Meanwhile, in a glovebox, 4 mmol of Se (316 mg), 3.32 g of TOP, and 5.49 g of ODE were stirred until all the Se dissolved and then loaded into a syringe. The contents of the syringe were rapidly injected into the Cd-oleate solution at 210 °C and allowed to react for 20 min under argon. The samples were cooled to room temperature and cleaned twice in air by precipitating the nanocrystals with ethanol and centrifuged at 8000 rpm. The resulting pellet was dissolved in hexanes. Samples were transferred to a glovebox and stored in hexanes. The concentration of the nanocrystal solution was determined photometrically using known size-dependent extinction coefficients (*45*).

*Synthesis of long* $\{\acute{1}100\}$*-terminated CdSe nanorods (Fig. 3, fig. S23-S24).* 400 $\mu$L of OA, 412 $\mu$L of OAm, 40 mg of CTAC and 5 ml of dioctyl ether were loaded to a 25 ml three-neck round bottom flask were degassed at room temperature. Next CdSe seeds were added (0.125 mmol of Cd-equivalents) as a solution in hexanes. Next the flask was evacuated to remove residual hexanes followed by heating to 50 °C under vacuum. Next the sample was heated to 260 °C under argon and after reacting for 20 min at the reaction temperature, the sample was cooled to room temperature. The particles were precipitated twice using the ethanol/hexanes non-solvent/solvent pair. The nanocrystals were stored in hexanes in an Ar filled glovebox. The static TEM characterization is shown in fig. S14.

*Synthesis of long* $\{11\acute{2}0\}$*-terminated CdSe nanorods (fig. S27-S28).* 400 $\mu$L of OA, 412 $\mu$L of OAm, 40 mg of CTAC and 5 ml of dioctyl ether were loaded to a 25 ml three-neck round bottom flask were degassed at room temperature. Next CdSe seeds were added (0.125 mmol of Cd-equivalents) as a solution in hexanes. Next the flask was evacuated to remove residual hexanes followed by heating to 50 °C under vacuum. Next the sample was heated to 280 °C under argon and after reacting for 20 min at the reaction temperature, the sample was cooled to room temperature. The particles were precipitated twice using the ethanol/hexanes non-solvent/solvent pair. The nanocrystals were stored in hexanes in an Ar filled glovebox. The static TEM characterization is shown in fig. S14.

*Synthesis of short* $\{\acute{1}100\}$*-terminated CdSe nanodisks (Fig. 4, fig. S30).* 800 $\mu$L of OA, 800 $\mu$L of OAm, 160 mg of CTAC and 10 ml of dibenzyl ether were loaded into a 25 ml three-neck round bottom flask. The contents of the flask were degassed at room temperature. Next CdSe seeds were added (0.25 mmol of Cd-equivalents) as a solution in hexanes. Next the flask was evacuated to remove residual hexanes followed by heating to 50 °C under vacuum. The flask was switched to argon and heated to 295 °C. After 22 min at 295 °C, the flask was cooled to room temperature. The particles were precipitated twice using the ethanol/hexanes non-solvent/solvent pair. The nanocrystals were stored in hexanes in an Ar filled glovebox. The static TEM characterization is shown in fig. S29.

*Structural characterization.* X-ray diffraction (XRD) data was collected on a Bruker D2 Phaser instrument operating with Cu K-alpha x-rays with a wavelength of 1.5418 Å. The bright-field transmission electron microscopy (TEM) images of the synthesized nanocrystals were obtained using a 200 kV FEI Tecnai G2 T20 S-TWIN microscope with a Gatan RIO16-IS camera. The aberration-corrected high-angle annular dark-field scanning transmission electron microscopy (AC-HAADF-STEM) images of the CdSe nanorods were obtained on the TEAM 0.5 microscope at the Molecular Foundry of the Lawrence Berkeley National Laboratory. Images were acquired at 300kV with a convergence semi-angle of 17 mrad, a beam current of

approximately 70 pA, and HAADF detector inner/outer angle of 44 to 222 mrad. Detailed structural analysis regarding the lattice polarity and 3D models of CdSe nanorods is included in fig. S15-S22.

**Preparation of liquid cells for *in-situ* TEM experiments**

We used the ultra-thin carbon films supported on 400 mesh gold grids (Electron Microscopy Sciences, CF400-Au-UL) to encapsulate the liquid and nanocrystals. 10 mM Tris·HCl solution was prepared by dissolving tris(hydroxymethyl)aminomethane hydrochloride (Fisher Scientific, AC228031000, >99%) in water (Milli-Q, 18.2 MΩ). Prior to making a liquid cell, the TEM grids were placed onto a clean glass slide with the carbon-coated side facing downward. Then the glass slide was transferred to a low-pressure chamber and cleaned with air plasma for ~10 seconds.

A pair of cleaned TEM grids including a bottom grid and a top grid were used for fabricating a liquid cell. The nanocrystals and the liquid droplet were loaded in two separated steps. First, a dilute solution of nanocrystals in hexanes was transferred outside of the Ar-filled glovebox, and ~5 μL of the solution was pipetted onto the carbon-coated side of a TEM grid to which we referred as the bottom grid. Most of the hexanes evaporated within a few seconds. The residual solvent on the bottom grid was further removed by pumping in a vacuum desiccator for an hour. As for the top grid, we cut a fraction of it using a razor blade. The top grid without nanocrystals was stored alongside the bottom grid in the vacuum desiccator. Next, both the bottom and top grids were transferred out of the desiccator. The bottom grid loaded with the nanocrystals was picked up with a self-closing tweezer holding the edge of the grid. The carbon-coated side of the bottom grid was facing upwards. A small droplet, ~0.1 μL in volume, of the Tris·HCl solution was pipetted onto the center of the carbon-coated side of the bottom grid. Then we quickly and carefully placed the partially cut top grid on top of the bottom grid, with the carbon-coated side of the top grid facing downwards, to encapsulate the droplet. The holding point between the bottom grid and the self-closing tweezer would not prevent the top and bottom grids from forming a close contact since we had cut a fraction of the top grid.

After 5-10 minutes, a stable seal had formed between the top and bottom grids. The liquid sealed between the two grids is thin enough to form high resolution electron micrographs. We then loaded the grid pair containing the nanoscale liquid pockets into a standard TEM holder, and proceeded for *in-situ* observations.

For Movie S8, 10 mM aqueous solution of tris(hydroxymethyl)aminomethane hemisulfate (Tris·0.5$H_2SO_4$) was used instead of the Tris·HCl solution. The 10 mM Tris·0.5$H_2SO_4$ solution was prepared by mixing a 20 mM tris(hydroxymethyl)aminomethane (Tris base, Millipore, 648311, >99%) solution and a 10 mM sulfuric acid solution at 1:1 v/v ratio, and the final pH was verified as 5.0.

**Liquid cell TEM (LCTEM) experiments**

All of the LCTEM experiments were performed on a 200 kV FEI Tecnai G2 T20 S-TWIN microscope with a Gatan RIO camera at 2048 x 2048 resolution. The nominal magnification of 145 kX corresponds to a pixel resolution of 0.926 Å/pixel. The electron fluence rate applied at each experiment was calibrated using a previously published protocol which was described with details (*21*, *46*). The factor for relating the camera counts to the number of incident electrons is 124 counts per electron. For the electron fluence rate of 400 or 800 $e^{-}\cdot Å^{-2}\cdot s^{-1}$, the videos were recorded at a frame rate of 4 fps. For faster etching occurred under the fluence rate of 2000 $e^{-}\cdot Å^{-2}\cdot s^{-1}$, the videos were recorded at frame rates ranging from 6 to 15 fps to balance the temporal resolution and the exposure time required to provide high quality images.

The thin liquid pockets were randomly distributed in the two-dimensional space between the two grids. The fluence rate was initially set to very low values (<10 $e^{-}\cdot Å^{-2}\cdot s^{-1}$) so that we can search for liquid pockets containing nanocrystals without triggering the etching processes. Once such pockets were found, we first started the recording, and then raised the fluence rate to a desired value that initiated the etching processes. This method ensured the capture of complete etching trajectories of individual nanocrystals. In all the videos, time zero refers to the moment when the fluence rate is raised to the desired value for etching. Table S5 contains a list of the all the LCTEM movies included here and their collection parameters.

**Image analysis**

LCTEM videos were analyzed using the MATLAB software. Each frame of a video acquired in the format of .dm4 raw file was loaded into MATLAB and re-saved as a TIFF file. Further image analysis was performed on the TIFF files. The grayscale intensity at each pixel of the TIFF files was kept proportional to the calibrated fluence rate registered at each pixel in the .dm4 files. This allows us to analyze and compare the electron fluence rates detected at different regions of the image. For each TIFF file, a script was used to threshold and outline the projected shape of the nanocrystal from background (*17*, *46*). Once the outlines were obtained, local curvature for each point of the outline can be calculated. The Fourier transform of the LCTEM images were performed using the Gatan DigitalMicrograph 3 software.

**Pulse radiolysis experiments**

The pulse radiolysis experiments were carried out using 15 ns electron pulses from the 10 MeV linear accelerator Elektronika-U003 (Toriy, Moscow). The dose delivered per pulse was measured by electron dosimetry and SCN dosimetry. Doses of 30 and 85 Gy/pulse, which correspond to fluence rates of 910 and 2570 $e^{-}\cdot Å^{-2}\cdot s^{-1}$, respectively, were applied. The conversion method had been previously published by Schneider *et al.* (*22*). The optical detection system consisted of a pulsed 1000 W xenon lamp (Osram, XBO1000), Suprasil cell (light path 1 cm), high-intensity grating monochromator (Acton research, SP500), R928 photomultiplier (Hamamatsu Photonics), and a fast transient recorder (Tektronix, TDS5034B). Linac operation and data acquisition were done in the computer-controlled mode.

**References**


1. A. P. Alivisatos, Semiconductor clusters, nanocrystals, and quantum dots. *Science* **271**, 933–937 (1996).

2. C. B. Murray, D. J. Norris, M. G. Bawendi, Synthesis and characterization of nearly monodisperse CdE (E = sulfur, selenium, tellurium) semiconductor nanocrystallites. *J. Am. Chem. Soc.* **115**, 8706–8715 (1993).

3. L. E. Brus, Electron–electron and electron-hole interactions in small semiconductor crystallites: The size dependence of the lowest excited electronic state. *J. Chem. Phys.* **80**, 4403–4409 (1984).

4. A. P. Alivisatos, W. Gu, C. Larabell, Quantum dots as cellular probes. *Annu. Rev. Biomed. Eng.* **7**, 55–76 (2005).

5. D. A. Hanifi, N. D. Bronstein, B. A. Koscher, Z. Nett, J. K. Swabeck, K. Takano, A. M. Schwartzberg, L. Maserati, K. Vandewal, Y. van de Burgt, A. Salleo, Redefining near-unity luminescence in quantum dots with photothermal threshold quantum yield. A. P.

Alivisatos, *Science* **363**, 1199–1202 (2019).

6. O. V. Kozlov, Y.-S. Park, J. Roh, I. Fedin, T. Nakotte, V. I. Klimov, Sub–single-exciton lasing using charged quantum dots coupled to a distributed feedback cavity. *Science* **365**, 672–675 (2019).

7. Y.-H. Won, O. Cho, T. Kim, D.-Y. Chung, T. Kim, H. Chung, H. Jang, J. Lee, D. Kim, E. Jang, Highly efficient and stable InP/ZnSe/ZnS quantum dot light-emitting diodes. *Nature*. **575**, 634–638 (2019).

8. O. Chen, J. Zhao, V. P. Chauhan, J. Cui, C. Wong, D. K. Harris, H. Wei, H.-S. Han, D. Fukumura, R. K. Jain, M. G. Bawendi, Compact high-quality CdSe–CdS core–shell nanocrystals with narrow emission linewidths and suppressed blinking. *Nat. Mater.* **12**, 445–451 (2013).

9. M. A. Gosálvez, I. Zubel, E. Viinikka, "Wet etching of silicon" in *Handbook of Silicon Based MEMS Materials and Technologies (Micro and Nano Technologies),* M. Tilli, M. Paulasto-Krockel, M. Petzold, H. Theuss, T. Motooka, V. Lindroos, Eds. (Elsevier, ed. 2, 2015), chap. 22, pp. 470–502.

10. M. H. Oh, M. G. Cho, D. Y. Chung, I. Park, Y. P. Kwon, C. Ophus, D. Kim, M. G. Kim, B. Jeong, X. W. Gu, J. Jo, J. M. Yoo, J. Hong, S. McMains, K. Kang, Y.-E. Sung, A. P. Alivisatos, T. Hyeon, Design and synthesis of multigrain nanocrystals via geometric misfit strain. *Nature*. **577**, 359–363 (2020).

11. M. A. Boles, D. Ling, T. Hyeon, D. V Talapin, The surface science of nanocrystals. *Nat. Mater.* **15**, 141–153 (2016).

12. J. J. Calvin, A. S. Brewer, A. P. Alivisatos, The role of organic ligand shell structures in colloidal nanocrystal synthesis. *Nat. Synth.* **1**, 127–137 (2022).

13. Z. Ou, Z. Wang, B. Luo, E. Luijten, Q. Chen, Kinetic pathways of crystallization at the nanoscale. *Nat. Mater.* **19**, 450–455 (2020).

14. V. Jamali, C. Hargus, A. Ben-Moshe, A. Aghazadeh, H. D. Ha, K. K. Mandadapu, A. P. Alivisatos, Anomalous nanoparticle surface diffusion in LCTEM is revealed by deep learning-assisted analysis. *Proc. Natl. Acad. Sci. USA* **118**, e2017616118 (2021).

15. S. Jeon, T. Heo, S.-Y. Hwang, J. Ciston, K. C. Bustillo, B. W. Reed, J. Ham, S. Kang, S. Kim, J. Lim, K. Lim, J. S. Kim, M.-H. Kang, R. S. Bloom, S. Hong, K. Kim, A. Zettl, W. Y. Kim, P. Ercius, J. Park, W. C. Lee, Reversible disorder-order transitions in atomic crystal nucleation. *Science* **371**, 498–503 (2021).

16. M. J. Williamson, R. M. Tromp, P. M. Vereecken, R. Hull, F. M. Ross, Dynamic microscopy of nanoscale cluster growth at the solid–liquid interface. *Nat. Mater.* **2**, 532–536 (2003).

17. X. Ye, M. R. Jones, L. B. Frechette, Q. Chen, A. S. Powers, P. Ercius, G. Dunn, G. M. Rotskoff, S. C. Nguyen, V. P. Adiga, A. Zettl, E. Rabani, P. L. Geissler, A. P. Alivisatos, Single-particle mapping of nonequilibrium nanocrystal transformations. *Science* **354**, 874–877 (2016).

18. M. F. Crook, C. Laube, I. A. Moreno-Hernandez, A. Kahnt, S. Zahn, J. C. Ondry, A. Liu, A. P. Alivisatos, Elucidating the role of halides and iron during radiolysis-driven oxidative

etching of gold nanocrystals using liquid cell transmission electron microscopy and pulse radiolysis. *J. Am. Chem. Soc.* **143**, 11703–11713 (2021).

19. I. A. Moreno-Hernandez, M. F. Crook, J. C. Ondry, A. P. Alivisatos, Redox mediated control of electrochemical potential in liquid cell electron microscopy. *J. Am. Chem. Soc.* **143**, 12082–12089 (2021).

20. W. Yu, P. Xinxing, A. Alex, X. Penghao, Q. Caroline, Y. Lei, O. Colin, E. Peter, W. Lin-Wang, L. Matt, Z. Haimei, Dynamic deformability of individual PbSe nanocrystals during superlattice phase transitions. *Sci. Adv.* **5**, eaaw5623 (2021).

21. M. R. Hauwiller, J. C. Ondry, C. M. Chan, P. Khandekar, J. Yu, A. P. Alivisatos, Gold nanocrystal etching as a means of probing the dynamic chemical environment in graphene liquid cell electron microscopy. *J. Am. Chem. Soc.* **141**, 4428–4437 (2019).

22. N. M. Schneider, M. M. Norton, B. J. Mendel, J. M. Grogan, F. M. Ross, H. H. Bau, Electron–water interactions and implications for liquid cell electron microscopy. *J. Phys. Chem. C*. **118**, 22373–22382 (2014).

23. T. J. Woehl, P. Abellan, Defining the radiation chemistry during liquid cell electron microscopy to enable visualization of nanomaterial growth and degradation dynamics. *J. Microsc.* **265**, 135–147 (2017).

24. P. Wardman, Reduction potentials of one-electron couples involving free radicals in aqueous solution. *J. Phys. Chem. Ref. Data*. **18**, 1637–1755 (1989).

25. M. Jonsson, D. D. M. Wayner, J. Lusztyk, Redox and acidity properties of alkyl- and arylamine radical cations and the corresponding aminyl radicals. *J. Phys. Chem.* **100**, 17539–17543 (1996).

26. R. Li, J. Lee, B. Yang, D. N. Horspool, M. Aindow, F. Papadimitrakopoulos, Amine-assisted facetted etching of CdSe nanocrystals. *J. Am. Chem. Soc.* **127**, 2524–2532 (2005).

27. S. Chen, L.-W. Wang, Thermodynamic oxidation and reduction potentials of photocatalytic semiconductors in aqueous solution. *Chem. Mater.* **24**, 3659–3666 (2012).

28. W. Lu, J. Fang, Y. Ding, Z. L. Wang, Formation of PbSe nanocrystals: A growth toward nanocubes. *J. Phys. Chem. B*. **109**, 19219–19222 (2005).

29. H. Li, D. Chen, L. Li, F. Tang, L. Zhang, J. Ren, Size- and shape-controlled synthesis of PbSe and PbS nanocrystals via a facile method. *CrystEngComm*. **12**, 1127–1133 (2010).

30. G. A. Somorjai, *Chemistry in Two Dimensions: Surfaces*. (Cornell University Press, Ithaca, NY, 1981).

31. D. J. Hellebusch, K. Manthiram, B. J. Beberwyck, A. P. Alivisatos, *In Situ* transmission electron microscopy of cadmium selenide nanorod sublimation. *J. Phys. Chem. Lett.* **6**, 605–611 (2015).

32. M. A. van Huis, N. P. Young, G. Pandraud, J. F. Creemer, D. Vanmaekelbergh, A. I. Kirkland, H. W. Zandbergen, Atomic imaging of phase transitions and morphology transformations in nanocrystals. *Adv. Mater.* **21**, 4992–4995 (2009).

33. X. Peng, L. Manna, W. Yang, J. Wickham, E. Scher, A. Kadavanich, A. P. Alivisatos,

Shape control of CdSe nanocrystals. *Nature*. **404**, 59–61 (2000).

34. A. R. Tao, S. Habas, P. Yang, Shape control of colloidal metal nanocrystals. *Small*. **4**, 310–325 (2008).

35. Y. Xia, X. Xia, H.-C. Peng, Shape-Controlled synthesis of colloidal metal nanocrystals: Thermodynamic versus kinetic products. *J. Am. Chem. Soc.* **137**, 7947–7966 (2015).

36. P. K. Jain, L. Amirav, S. Aloni, A. P. Alivisatos, Nanoheterostructure Cation Exchange: Anionic Framework Conservation. *J. Am. Chem. Soc.* **132**, 9997–9999 (2010).

37. L. Manna, E. C. Scher, A. P. Alivisatos, Synthesis of soluble and processable rod-, arrow-, teardrop-, and tetrapod-shaped CdSe nanocrystals. *J. Am. Chem. Soc.* **122**, 12700–12706 (2000).

38. M. G. Burt, J. H. Harding, A. M. Stoneham, E. C. Scher, L. Manna, A. P. Alivisatos, Shape control and applications of nanocrystals. *Philos. Trans. R. Soc. London. A* **361**, 241–257 (2003).

39. J. C. Ondry, A. P. Alivisatos, Application of dislocation theory to minimize defects in artificial solids built with nanocrystal building blocks. *Acc. Chem. Res.* **54**, 1419–1429 (2021).

40. J. C. Ondry, J. P. Philbin, M. Lostica, E. Rabani, A. P. Alivisatos, Resilient pathways to atomic attachment of quantum dot dimers and artificial solids from faceted CdSe quantum dot building blocks. *ACS Nano*. **13**, 12322–12344 (2019).

41. M. Saruyama, M. Kanehara, T. Teranishi, Drastic structural transformation of cadmium chalcogenide nanoparticles using chloride ions and surfactants. *J. Am. Chem. Soc.* **132**, 3280–3282 (2010).

42. D. J. Eaglesham, A. E. White, L. C. Feldman, N. Moriya, D. C. Jacobson, Equilibrium shape of Si. *Phys. Rev. Lett.* **70**, 1643–1646 (1993).

43. C. Messmer, J. C. Bilello, The surface energy of Si, GaAs, and GaP. *J. Appl. Phys.* **52**, 4623–4629 (1981).

44. M. R. Hauwiller, X. Ye, M. R. Jones, C. M. Chan, J. J. Calvin, M. F. Crook, H. Zheng, A. P. Alivisatos, Tracking the effects of ligands on oxidative etching of gold nanorods in graphene liquid cell electron microscopy. *ACS Nano*. **14**, 10239–10250 (2020).

45. W. W. Yu, L. Qu, W. Guo, X. Peng, Experimental determination of the extinction coefficient of CdTe, CdSe, and CdS nanocrystals. *Chem. Mater.* **15**, 2854–2860 (2003).

46. M. R. Hauwiller, L. B. Frechette, M. R. Jones, J. C. Ondry, G. M. Rotskoff, P. Geissler, A. P. Alivisatos, Unraveling kinetically-driven mechanisms of gold nanocrystal shape transformations using graphene liquid cell electron microscopy. *Nano Lett.* **18**, 5731–5737 (2018).

47. G. V. Buxton, "Radiation Chemistry of the Liquid State: (1) Water and Homogeneous Aqueous Solutions" in *Radiation Chemistry: Principles and Applications,* Farhataziz, M. A. J. Rodgers, Eds. (VCH Pub., Weinheim, 1988), chap. 10, pp. 321–349.

48. G. V Buxton, C. L. Greenstock, W. P. Helman, A. B. Ross, Critical review of rate constants for reactions of hydrated electrons, hydrogen atoms and hydroxyl radicals (·OH/ ·$O^-$ in aqueous solution. *J. Phys. Chem. Ref. Data*. **17**, 513–886 (1988).

49. K. P. Madden, S. P. Mezyk, Critical review of aqueous solution reaction rate constants for hydrogen atoms. *J. Phys. Chem. Ref. Data*. **40**, 023103 (2011).

50. G. G. Jayson, B. J. Parsons, A. J. Swallow, Some simple, highly reactive, inorganic chlorine derivatives in aqueous solution. Their formation using pulses of radiation and their role in the mechanism of the Fricke dosimeter. *J. Chem. Soc. Faraday Trans.* **69**, 1597–1607 (1973).

51. E. Hayon, A. Treinin, J. Wilf, Electronic spectra, photochemistry, and autoxidation mechanism of the sulfite-bisulfite-pyrosulfite systems. $SO_2^-$, $SO_3^-$, $SO_4^-$, and $SO_5^-$ radicals. *J. Am. Chem. Soc.* **94**, 47–57 (1972).

52. M. Schmittel, A. Burghart, Understanding reactivity patterns of radical cations. *Angew. Chemie Int. Ed.* **36**, 2550–2589 (1997).

53. B. H. J. Bielski, D. E. Cabelli, R. L. Arudi, A. B. Ross, Reactivity of $HO_2/O^-_2$ radicals in aqueous solution. *J. Phys. Chem. Ref. Data*. **14**, 1041–1100 (1985).

54. A. J. Elliot, D. R. McCracken, Computer modelling of the radiolysis in an aqueous lithium salt blanket: Suppression of radiolysis by addition of hydrogen. *Fusion Eng. Des.* **13**, 21–27 (1990).

55. D. A. Armstrong, R. E. Huie, S. Lymar, W. H. Koppenol, G. Merényi, P. Neta, D. M. Stanbury, S. Steenken, P. Wardman, Standard electrode potentials involving radicals in aqueous solution: inorganic radicals. *Bioinorg. React. Mech.* **9**, 59–61 (2013).

56. A. J. Bard, R. Parsons, J. Jordan, International Union of Pure and Applied Chemistry, *Standard Potentials in Aqueous Solution* (Monographs in Electroanalytical Chemistry and Electrochemistry, M. Dekker, New York, 1985).

57. A. K. El Omar, U. Schmidhammer, B. Rousseau, J. LaVerne, M. Mostafavi, Competition reactions of $H_2O^{\bullet+}$ radical in concentrated $Cl^-$ aqueous solutions: Picosecond pulse radiolysis study. *J. Phys. Chem. A*. **116**, 11509–11518 (2012).

58. E. Bjergbakke, S. Navaratnam, B. J. Parsons, A. J. Swallow, Reaction between hydroperoxo radicals and chlorine in aqueous solution. *J. Am. Chem. Soc.* **103**, 5926–5928 (1981).

59. P.-Y. Jiang, Y. Katsumura, R. Nagaishi, M. Domae, K. Ishikawa, K. Ishigure, Y. Yoshida, Pulse radiolysis study of concentrated sulfuric acid solutions. Formation mechanism, yield and reactivity of sulfate radicals. *J. Chem. Soc. Faraday Trans.* **88**, 1653–1658 (1992).

**Acknowledgements:**

**Funding:** This work was supported by the U.S. Department of Energy, Office of Science, Office of Basic Energy Sciences, Materials Sciences and Engineering Division, under Contract No. DE-

AC02-05-CH11231 within the Physical Chemistry of Inorganic Nanostructures Program (KC3103). Work at the Molecular Foundry was supported by the Office of Science, Office of Basic Energy Sciences, of the U.S. Department of Energy under Contract No. DE-AC02-05-CH11231. J.C.O. gratefully acknowledges the support of the Kavli Philomathia Graduate Student Fellowship. Contributions by I. A. M.-H. were supported by the "Photonics at Thermodynamic Limits" Energy Frontier Research Center funded by the U. S. Department of Energy (DOE), Office of Science, Office of Basic Energy Sciences, under award DE-SC0019140.

**Author contributions**: A.P.A., C.Y., and J.C.O. conceptualized the project. C.Y., D.B., J.C.O., A.K., G.A.K., Z.-J.L., C.L., and P.E. performed experiments. C.Y., D.B., and G.A.K. collected and analyzed the LCTEM data. C.Y., J.C.O., and Z.-J.L. synthesized the nanocrystals. A.K. and C.L. performed pulse radiolysis experiments and processed the radiolysis data. I.A.M.-H. performed the modeling on radiolysis reactions. P.E. collected the AC-HAADF-STEM images and J.C.O. analyzed the images. I.A.M.-H., M.F.C., and Y.Z. contributed to 3D graphical design. C.Y., D.B., J.C.O., A.K., I.A.M.-H., and A.P.A. wrote the manuscript. All authors read and commented on the manuscript.

**Competing interests:** Authors declare that they have no competing interests.

**Data and materials availability:** All data are available in the main text or the supplementary materials.

## Supplementary Materials

Supplementary Text

Figs. S1 to S30

Tables S1 to S5

References (47–59)

Movies S1 to S8

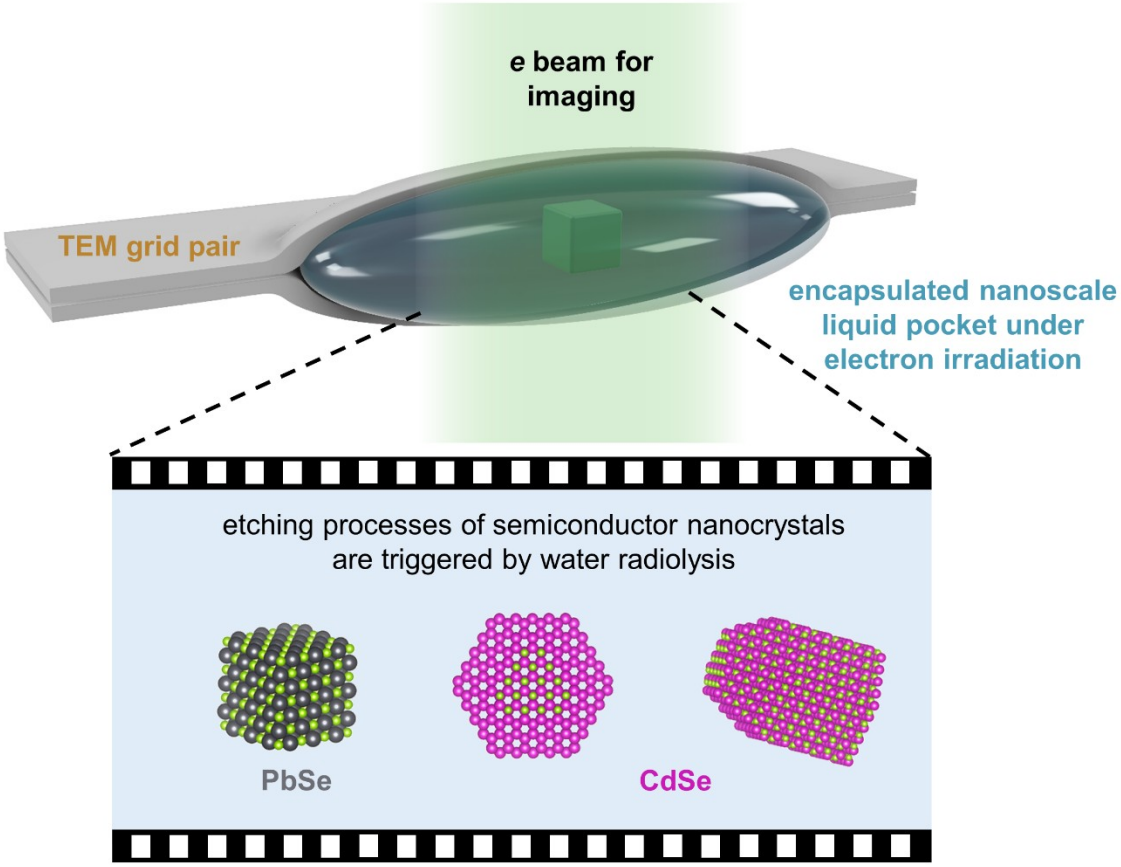


**Fig. 1. Illustration of the LCTEM experiments.** The cross-sectional view shows that a thin aqueous layer containing semiconductor nanocrystals is sandwiched between two ultrathin carbon films of a pair of TEM grids. The electron beam passing through the water and the carbon layers causes water radiolysis reactions which then trigger the etching trajectories to be imaged with LCTEM.

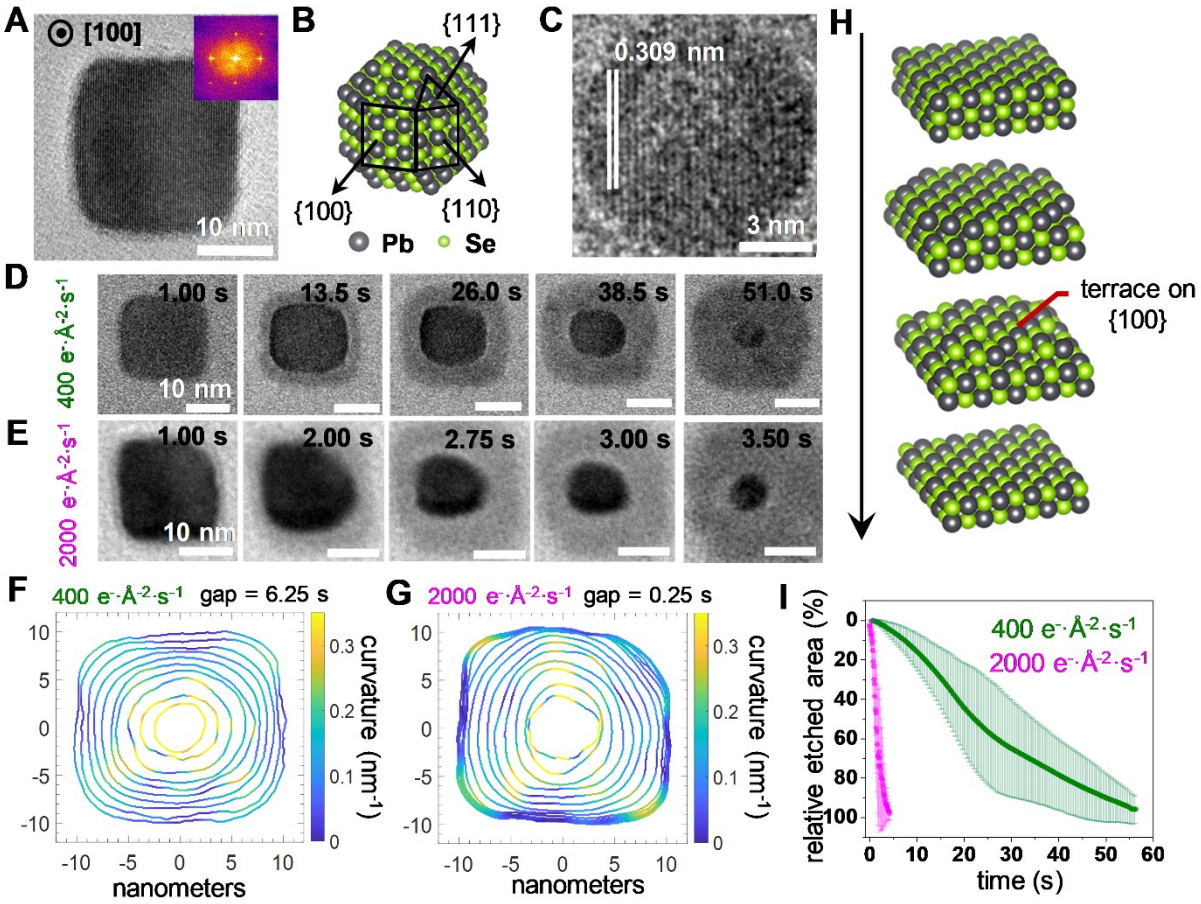


**Fig. 2. Structural characterization and etching trajectories of PbSe nanocubes. (A)** Representative static TEM image of a PbSe nanocube oriented along the [100] zone axis. **(B)** Atomistic model of a truncated PbSe nanocube exposing different facets. **(C)** The LCTEM image captured near the end of an etching trajectory, exhibiting the characteristic *d*-spacing of {200} lattice planes of PbSe. **(D-E)** Time-lapse LCTEM images recorded at the electron fluence rates of 400 $e^{-}\cdot Å^{-2}\cdot s^{-1}$ (D), and 2000 $e^{-}\cdot Å^{-2}\cdot s^{-1}$ (E), respectively. **(F-G)** Outlines of the nanocrystals plotted with equal time gaps for illustrating the evolving shapes and local curvatures of PbSe nanocrystals recorded at 400 $e^{-}\cdot Å^{-2}\cdot s^{-1}$ (F), and 2000 $e^{-}\cdot Å^{-2}\cdot s^{-1}$ (G), respectively. **(H)** Scheme of the layer-by-layer etching mechanism which proceeds via terrace intermediates. **(I)** The time-dependent plots of the relative etched area normalized to the projected area of the PbSe nanocube at the starting frame.

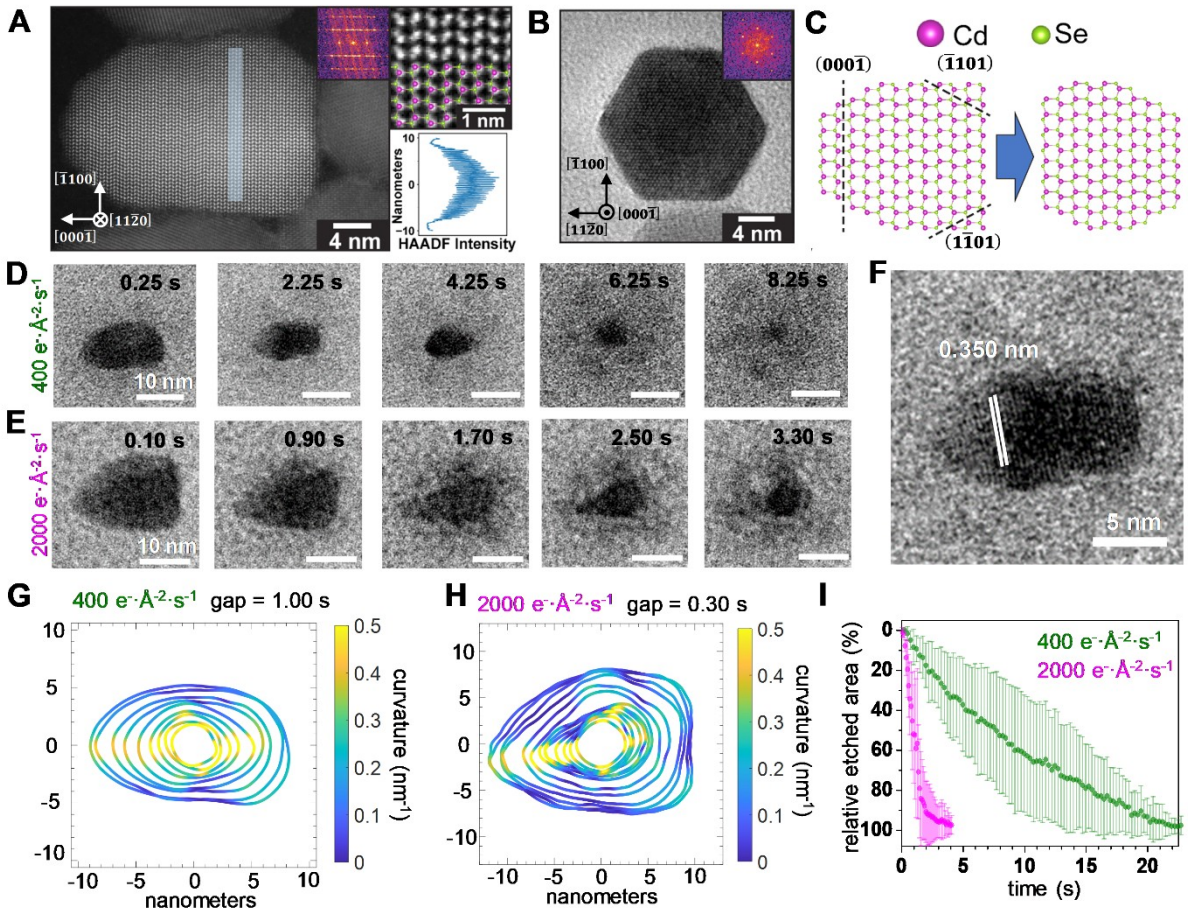


**Fig. 3. Structural characterization and etching trajectories of CdSe nanorods. (A)** AC-HAADF-STEM image of a wurtzite CdSe nanorod projected along the [11$\acute{2}$0] zone axis (left). The enlarged inset (upper right) verifies the polarity of the nanorod: the tip of the rod is terminated by Se (green) while the bottom is terminated by Cd (pink). The line profile of HAADF-STEM intensity in the shaded segment (left panel) projected along the [$\acute{1}$ 100] axis is included in the lower right panel. **(B)** TEM image of a nanorod oriented along the *c*-axis showing a hexagonal projection. **(C)** Lattice models of a CdSe nanorod projected along the [11$\acute{2}$0] axis (left) and the truncated structure (right) formed by selectively etching the Se-terminated facets. **(D-E)** Time-lapse LCTEM images recorded at electron fluence rates of 400 $e^{-}\cdot Å^{-2}\cdot s^{-1}$ (D), and 2000 $e^{-}\cdot Å^{-2}\cdot s^{-1}$ (E), respectively. **(F)** The LCTEM image exhibiting the characteristic *d*-spacing of {0002} lattice planes. **(G-H)** Outlines of the nanocrystals plotted with equal time gaps for illustrating the evolving shapes and local curvatures of CdSe nanorods at 400 $e^{-}\cdot Å^{-2}\cdot s^{-1}$ (G), and 2000 $e^{-}\cdot Å^{-2}\cdot s^{-1}$ (H), respectively. **(I)** Time-dependent plots of the relative etched area normalized to the projected area of the CdSe nanorod at the starting frame.

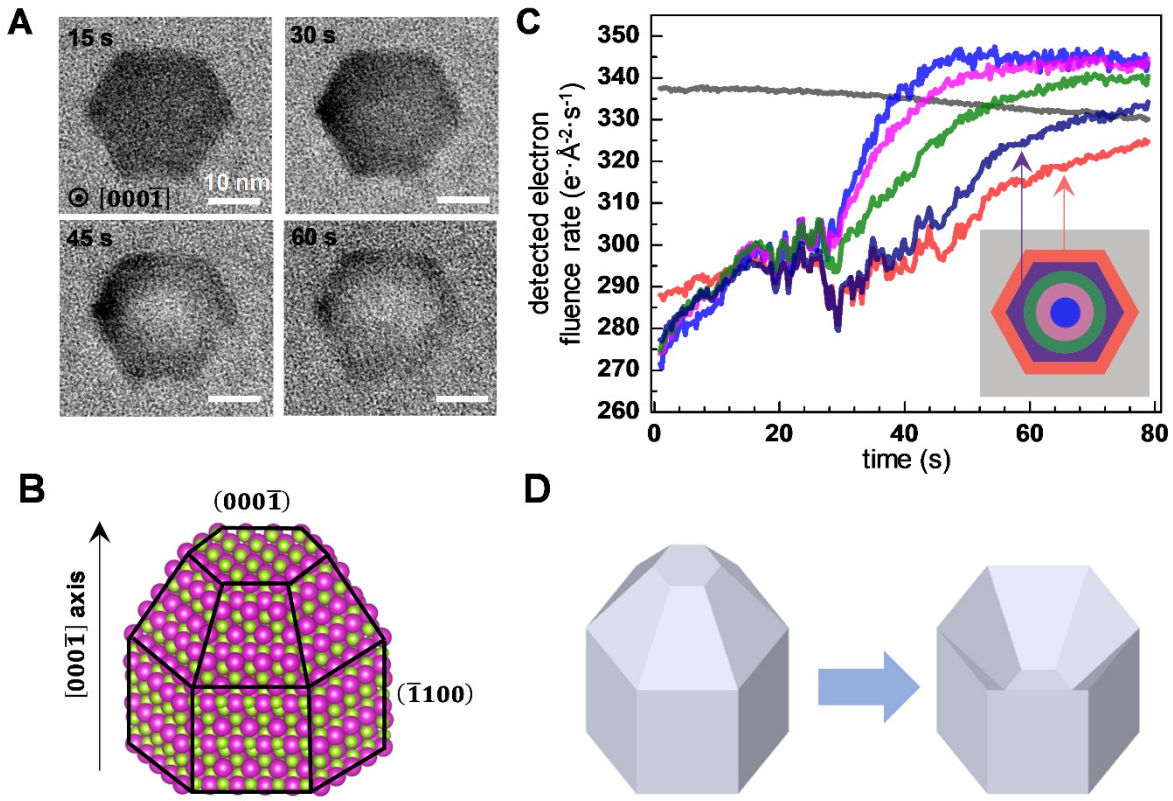


729 **Fig. 4. The etching trajectory of a wurtzite CdSe nanocrystal viewed along the [000$\acute{1}$] axis.**

730 **(A)** Time-lapse LCTEM images recorded at 400 $e^{-}\cdot Å^{-2}\cdot s^{-1}$. **(B)** Atomistic model of the CdSe
731 nanocrystal with the (000$\acute{1}$) facet pointing up. **(C)** Time-dependent plot of the average electron
732 fluence rates detected in different color-coded segments (inset) of the LCTEM images. Gray color
733 corresponds to the background region surrounding the nanocrystal. **(D)** 3D illustration of the
734 etching process showing the selective etching of the Se-terminated (000$\acute{1}$) facet causes the tip to
735 transform into a concave pit in the nanocrystal.
736

# Supplementary Materials for

## Facet-Selective Etching Trajectories of Individual Semiconductor Nanocrystals

Chang Yan, Dana Byrne, Justin C. Ondry, Axel Kahnt, Ivan A. Moreno-Hernandez, Gaurav A. Kamat, Zi-Jie Liu, Christian Laube, Michelle F. Crook, Ye Zhang, Peter Ercius, and A. Paul Alivisatos

Correspondence to: paul.alivisatos@uchicago.edu

**This PDF file includes:**



**Other Supplementary Materials for this manuscript include the following:**

**Supplementary Texts**

Analysis of radiolysis reactions in LCTEM

*Overview of the radiolysis reactions in LCTEM.* The radiolysis of water yields three reactive intermediates, $e_{(aq)}^-$, $^\bullet H$ and $^\bullet OH$ besides molecular and ionic products ($H_2O_2$, $H_2$ and $H_3O^+$) (*47*, *48*). Among these species, $e_{(aq)}^-$ and $^\bullet H$ have a reducing character, whereas $^\bullet OH$ can participate in either oxidation reactions, radical additions or hydrogen abstraction reactions. Since the LCTEM experiments were conducted in air saturated water, $e_{(aq)}^-$ and $^\bullet H$ radical react rapidly with molecular oxygen to form $O_2^{\bullet-}$ and $HO_2^\bullet$, respectively (*24*, *49*). In comparison with the highly oxidizing standard electrochemical potential of $^\bullet OH$ (+1.9 V vs. NHE), $O_2^{\bullet-}$ and $HO_2^\bullet$ only have mild standard electrochemical potentials (~-0.3 V vs. NHE) (*24*). Thus their reactions are not further considered. Furthermore, the G-value (radiation yield) is small for $^\bullet H$ (0.5 $^\bullet H$ per 100 eV vs. 2.65 $^\bullet OH$ per 100 eV) (*47*).

The reactive $^\bullet OH$ can further react with dissolved species in water to generate long-lived species with high steady-state concentrations which account for the etching of semiconductor nanocrystals. To investigate what species are directly responsible for the etching of nanocrystals in the 10 mM solution of Tris·HCl used in LCTEM etching experiments, we substituted the 10 mM Tris·HCl solution with 10 mM Tris·0.5($H_2SO_4$) solution. The 10 mM solutions of Tris·HCl or Tris·0.5($H_2SO_4$) both have a pH ~5. The aqueous solutions of Tris·HCl or Tris·0.5($H_2SO_4$) consist of protonated $TrisH^+$ cation and $Cl^-$ or $SO_4^{2-}$ anion. With the 10 mM Tris·0.5($H_2SO_4$) solution, etching of PbSe was observed (Fig. S1 and Movie S8). Thus, whether the anion was chloride or sulfate, etching was observed. The results suggest that the presence of protonated $TrisH^+$ cation could be responsible for etching to occur under radiolysis. A plausible etching mechanism is that the $TrisH^+$ cation reacts with $^\bullet OH$ to form an organic radical that can further oxidize the selenide ions in PbSe or CdSe, leading to the dissolution of the nanocrystals.

To provide evidence for this mechanism, pulse radiolysis experiments and radiolysis modeling were carried out. The results showed that, upon the start of water radiolysis in the solution of Tris·HCl or Tris·0.5($H_2SO_4$), $TrisH^+$ cation reacts swiftly with $^\bullet OH$ via the hydrogen abstraction mechanism to form the oxidizing $Tris^{\bullet+}$ radical that etches the nanocrystals. Oxidative species generated from $Cl^-$ or $SO_4^{2-}$ anions, such as $Cl_2^{\bullet-}$ or $HSO_5^-$, are too low in concentration to be responsible for etching. The $Pb^{2+}$ or $Cd^{2+}$ cations in the nanocrystals eventually form compounds such as $PbCl_2$ or $CdCl_2{\bullet}HCl{\bullet}H_2O$ after etching as shown by the Fourier analysis of LCTEM images (Fig. S13 and Fig. S25). Though radicals generated from $Cl^-$ or $SO_4^{2-}$ are not directly responsible for the oxidative etching process, the solubility of these compounds as etching products and the complexation constants between the anions and the metal cations could impact the kinetics of the etching (*18*). The elucidation of the mechanism on how different anions such as halide ions or sulfate ions impact the etching processes of semiconductor nanocrystals requires further systematic studies which will not be included here.

The etching mechanism is summarized in Fig. S7. The results and analysis are included below with details.

*Pulse radiolysis experiments on the aqueous solutions of Tris and Tris·HCl.* Pulse radiolysis experiments with the fluence rates comparable to those used in LCTEM experiments were conducted to decipher potential reaction pathways of the organic species Tris and $TrisH^+$. It is important to measure the reaction kinetics involving the Tris base species since $TrisH^+$ exist in water in equilibrium with Tris. The obtained reaction rate constants involving Tris and $TrisH^+$ will be further used to simulate the reaction networks under electron radiolysis.

**(I).** First, we measured the reaction rate constants of Tris or Tris·HCl with $^\bullet OH$. $^\bullet OH$ was generated from water radiolysis by the following standard procedure. An aqueous solution

containing a known concentration of Tris or Tris·HCl was saturated with $N_2O$ and irradiated with the electron pulses. Under such conditions, solvated electrons formed during the radiolysis of water (eq. 1) were quenched and converted to $^{\bullet}OH$ (eq. 2) (*47*)

$$H_2O \rightsquigarrow e_{(aq)}^-, {}^{\bullet}H, {}^{\bullet}OH \qquad \text{(eq. 1)}$$

$$e_{(aq)}^- + H_2O + N_2O \rightarrow {}^{\bullet}OH + OH^- + N_2 \qquad \text{(eq. 2)}$$

$^{\bullet}OH$, which is a strong oxidizing intermediate with a standard electrochemical potential of + 1.9 V vs. NHE in neutral water (*24*), may react with Tris or $TrisH^+$ via an one-electron transfer mechanism, forming $OH^-$. Alternatively, $^{\bullet}OH$ may react with Tris or $TrisH^+$ via a hydrogen abstraction reaction (*48*), forming water.

For both the cases of Tris and Tris·HCl solutions, the transient absorption of the primary species of the water radiolysis were observed immediately after the electron pulse. These transient features decayed rapidly, giving rise to new transient absorption bands in the UV region of the optical spectrum. The transient absorption spectra of a Tris solution saturated with $N_2O$ were displayed in Fig. S2A, with time delays ranging from 100 ns to 2 μs. The spectra showed the formation of a distinct shoulder around 280 nm. The time-dependent transient absorbance at 280 nm (Fig. S2B) indicated that the reaction between Tris and $^{\bullet}OH$ was fast, and the reaction reached a steady state within ~1 μs.

In Fig. S2C, we showed the transient absorption spectra of a Tris·HCl solution saturated with $N_2O$. The reaction between Tris·HCl and $^{\bullet}OH$ formed transient absorption bands with a maximum around 300 nm and a transient bleaching around 260 nm. The time-dependent transient absorbance at 260 nm (Fig. S2D) indicated that the reaction between Tris·HCl and $^{\bullet}OH$ was also fast, and the reaction reached a steady state within ~1 μs.

Noteworthy is the finding that the transient absorption spectra did not provide any evidence for the formation of $Cl_2^{\bullet-}$ radicals, which have distinctively strong transient absorption features with a maximum around 360 nm (*50*). The data indicated that the reaction between Tris·HCl and $^{\bullet}OH$ is essentially the reaction between $TrisH^+$ and $^{\bullet}OH$. The reaction between $Cl^-$ and $^{\bullet}OH$ that leads to the formation of $Cl_2^{\bullet-}$ radicals (*50*) is too slow to compete with the fast reaction between $TrisH^+$ and $^{\bullet}OH$. $Cl^-$ and $TrisH^+$ have the same concentration. But the initial step of the reaction of $^{\bullet}OH$ with $Cl^-$ forming $ClOH^{\bullet-}$ is an equilibrium ($K_{eq}$=0.7) (*48*) so that the irreversible hydrogen abstraction reaction of $^{\bullet}OH$ with $TrisH^+$ can effectively prevent the formation of a sufficient concentration of $ClOH^{\bullet-}$. As a result, further reactions, such as $ClOH^{\bullet-} + H^+ \rightarrow H_2O + Cl^{\bullet}$ as well as $Cl^{\bullet} + Cl^- \rightarrow Cl_2^{\bullet-}$, hardly ever take place, and nearly no $Cl_2^{\bullet-}$ will be formed under pulse radiolysis conditions. The negligible concentration of $Cl_2^{\bullet-}$ is also verified by simulations discussed in the following section.

The curves in Fig. S2B and S2D exhibit pseudo-first-order kinetics that can be fitted with mono-exponential functions, of which the exponential rate constants are noted as $k_{obs}$. We measured $k_{obs}$ for a series of Tris or $TrisH^+$ concentrations. Fig. S3A showed the plot of $k_{obs}$ at 280 nm versus the concentration of Tris. A linear relationship between the observed pseudo-first-order rate constant and the concentration was obtained. As derived from the slope of the linear fit, the bimolecular rate constant of the reaction between Tris and $^{\bullet}OH$ is $3.4 \times 10^8$ L · mol$^{-1}$ · s$^{-1}$. Fig. S3B showed the plot of $k_{obs}$ at 260 nm versus the concentration of $TrisH^+$. Again, a linear relationship between $k_{obs}$ and the concentration was obtained. The bimolecular rate constant of the reaction between $TrisH^+$ and $^{\bullet}OH$ is determined as $9.8 \times 10^8$ L · mol$^{-1}$ · s$^{-1}$.

**(II).** To further decipher whether an oxidation reaction or a hydrogen abstraction reaction takes place between $^{\bullet}OH$ and the organic species, a set of reference experiments were conducted to examine the transient absorption of the product formed in the reaction between Tris or $TrisH^+$ and $SO_4^{\bullet-}$. $SO_4^{\bullet-}$ is a highly oxidative species (+2.4 V vs. NHE) (*24*), which is inert to hydrogen abstraction reaction mechanism and can only be reduced by electron transfer mechanism. If $^{\bullet}OH$

reacts with Tris or $TrisH^+$ in an electron transfer mechanism, the reaction kinetics and transient spectra of the product should be similar regardless of using $SO_4^{\bullet-}$ or $^\bullet OH$ as the reactant. If substantial differences in the transient absorption spectra were found between using $^\bullet OH$ and $SO_4^{\bullet-}$ as the reactant, the results would indicate that Tris or $TrisH^+$ reacts with $^\bullet OH$ via a hydrogen abstraction mechanism.

The formation of $SO_4^{\bullet-}$ by radiolysis necessitates the addition of $5\times10^{-2}$ M $K_2S_2O_8$ and 5 vol% *tert*-butanol (*t*-BuOH) to a $N_2$ saturated solution. The role of *t*-BuOH is to efficiently scavenge $^\bullet OH$ and $^\bullet H$ radicals (eq. 4). The $S_2O_8^{2-}$ reacts with $e_{(aq)}^-$ to form $SO_4^{2-}$ and $SO_4^{\bullet-}$ (eq. 5).

$$H_2O \rightsquigarrow e_{(aq)}^-,\ ^\bullet H,\ ^\bullet OH \qquad \text{(eq. 3)}$$

$$^\bullet OH\ (^\bullet H) + (CH_3)_3OH \rightarrow H_2O\ (H_2) + (^\bullet CH_2)(CH_3)_2OH \qquad \text{(eq. 4)}$$

$$e_{(aq)}^- + S_2O_8^{2-} \rightarrow SO_4^{\bullet-} + SO_4^{2-} \qquad \text{(eq. 5)}$$

In Fig. S4A, we showed the transient absorption spectra of the $N_2$ saturated 2 mM Tris solution containing $5\times10^{-2}$ M $K_2S_2O_8$ and 5 vol% *t*-BuOH. Right after the electron pulse, the characteristic transient absorption of $SO_4^{\bullet-}$ with its maximum around 440 nm was noticed (*51*). Comparing to the sub-μs fast kinetics of the reaction between Tris and $^\bullet OH$, the decay of this feature is relatively slow, lasting multiple μs (Fig. S4B). At long time, *e.g.* 20 μs, the remaining featureless transient absorption band also differs substantially in shape from the transient absorption band observed for the product of the reaction of Tris with $^\bullet OH$ (Fig. S2A). The fact that the reaction between Tris and $SO_4^{\bullet-}$ generated kinetics and spectra distinctive from those generated by the reaction between Tris and $^\bullet OH$ is a strong indication that Tris reacts with $^\bullet OH$ via hydrogen abstraction (eq. 6)

$$Tris + {}^\bullet OH \rightarrow Tris^\bullet + H_2O \qquad \text{(eq. 6)}$$

In Fig. S4C and S4D, we also observed that the reaction between Tris·HCl and $SO_4^{\bullet-}$ generated spectra distinctive from those generated by the reaction between Tris·HCl and $^\bullet OH$. Therefore, the reaction of $TrisH^+$ with $^\bullet OH$ shall also proceed via a hydrogen abstraction reaction mechanism (eq. 7).

$$TrisH^+ + {}^\bullet OH \rightarrow Tris^{\bullet+} + H_2O \qquad \text{(eq. 7)}$$

In summary, in LCTEM experiments, Tris and $TrisH^+$ both react with $^\bullet OH$ via hydrogen abstraction mechanism. Radical cations like $Tris^{\bullet+}$ are generally strong one-electron oxidizing intermediates (*25*, *52*) due to the electron-deficient nature. Thus $Tris^{\bullet+}$ shall account for the etching processes observed when using Tris·0.5($H_2SO_4$) or Tris·HCl as the additive. The reduction of $Tris^{\bullet+}$ by etching chalcogenide nanocrystals produces Tris, a stable molecular product. As shown in eq.8, Tris formed by the etching reaction can be recycled back to $TrisH^+$ when taking two facts into consideration: i) $H_3O^+$ is also formed as a product of the water radiolysis; ii) Tris is a stronger base (pKa = 8.2) than $HO_2^\bullet$ / $O_2^{\bullet-}$ (pKa = 4.8) (*53*).

$$Tris + H_3O^+ \rightarrow TrisH^+ + H_2O \qquad \text{(eq. 8)}$$

This recycling step ensures that, under the continuous irradiation during LCTEM experiments, even under-stoichiometric amounts of $TrisH^+$ can etch the nanocrystals completely over time via $Tris^{\bullet+}$ (Fig. S7).

*Modeling of radiolysis reactions in LCTEM.* The effects of chemical additives on liquid cell chemical reactivity were analyzed with a chemical kinetics model that has been previously developed. The modeling provides insights on the concentrations of various reactive species over a large time range under continuous electron radiation conditions which were used in the actual LCTEM experiments.

The model was described by Elliot and McCracken (*54*), and implemented in MATLAB for liquid cell electron microscopy conditions by Schneider *et al (22)*. The model contains 73 reactions for species derived from water, along with 31 reactions for chloride and sulfuric acid species. Reactions involving the organic additive, $TrisH^+$, and its derived species were included based on pulsed radiolysis studies presented herein and chemical equilibria. The hypothetical reactions of $Tris^{\bullet}$ and $Tris^{\bullet+}$ radicals reacting with atomic hydrogen were also included in this model, as these reactions could have substantial impact on the steady-state concentration of Tris and $TrisH^+$ radical species. The kinetic model was solved for homogenous concentration conditions by numerically solving a set of 110 coupled differential equations via MATLAB (eq. 9).

$$\frac{\partial C_i}{\partial t} = \sum_{j,k \neq i} k_{jk} C_j C_k - \sum_j k_{ij} C_i C_j + R_i \qquad \text{(eq. 9)}$$

Where $C_i$, $C_j$, and $C_k$ are the species concentrations, $k_{jk}$ and $k_{ij}$ are the reaction rate constants, and $R_i$ is the electron beam induced generation of species. The MATLAB implementation of this model is provided in the Alivisatos Github repository (*18*, *19*). The reactions beyond the 73 reactions of water radiolysis are listed in Table S3.

Fig. S5 shows the results from our chemical network model of the reactive environment under various electron fluence rates and chemical additive conditions. The fluence rates and additive conditions are listed in Table S4. In all cases the chemical network indicates that the predominant oxidizing species under electron irradiation is the radical cation, $Tris^{\bullet+}$. For an initial $TrisH^+$ concentration of 10 mM, the steady-state concentration of $Tris^{\bullet+}$ after 1 milli-second ranges from 7.8 to 8.5 mM, indicating that electron fluence and anions only have a minor effect on the steady-state concentration.

The steady-state concentrations of all the other redox species besides $Tris^{\bullet+}$ are in the nM and μM range so that they are not the primary reactants for etching nanocrystals in LCTEM. The concentrations of $Tris^{\bullet}$ radical are below 1 μM in all cases. The concentrations of hydroxyl radical are ~195 μM for all the solutions simulated at 400 $e^-\cdot Å^{-2}\cdot s^{-1}$, and ~480 μM for all the solutions simulated at 2000 $e^-\cdot Å^{-2}\cdot s^{-1}$. Similar behavior is observed for atomic hydrogen, with an increase in the steady-state concentration from 3.5 μM to 13 μM for an electron fluence increase from 400 $e^-\cdot Å^{-2}\cdot s^{-1}$ to 2000 $e^-\cdot Å^{-2}\cdot s^{-1}$. Oxidants generated from chloride or sulfate anions such as $Cl_2^{\bullet-}$ and $HSO_5^-$ have standard electrochemical potentials of 2.1 V (*23*, *55*) and 1.8 V (*56*) vs. SHE, respectively. However, $Cl_2^{\bullet-}$ and $HSO_5^-$, which have the highest steady-state concentrations among the anion-derived oxidants, are not the primary oxidants due to their low concentrations in the μM range as shown in Fig. S5, compared to the mM range expected for the $Tris^{\bullet+}$ species. The absence or very low concentration of $Cl_2^{\bullet-}$ radical has also been confirmed by the pulse radiolysis experiments discussed above.

Overall, the high steady-state concentration of $Tris^{\bullet+}$ and the standard electrochemical potentials for the one-electron reduction reactions of amine radical cations (0.83~1.34 V vs. SHE) suggests that $Tris^{\bullet+}$ is the primary oxidant for the conditions studied herein (*25*). The oxidative property of $Tris^{\bullet+}$ is sufficient to spontaneously etch the nanocrystals studied herein (*27*). As shown on Fig. S6, the pH and pOH of the solution at steady-state both decrease to the range of

3~5 as the result of water radiolysis, consistent with previous simulations for pure water in the liquid cell environment (*22*).

The exact standard electrochemical potential for the one-electron reduction of $Tris^{\bullet+}$ radical, as shown by eq. 10, is not accurately known, but is expected to be in the range of 0.83 V to 1.34 V vs. SHE based on published results for several amine radical cations (*25*). However, we can estimate the deviations from the standard electrochemical potential due to non-standard conditions using the Nernst equation. Radiolysis simulations indicate that at 400 $e^{-}\cdot Å^{-2}\cdot s^{-1}$, [$Tris^{\bullet+}$] = 8.41 mM and [Tris] = 0.12 mM, which would result in an electrochemical potential that is 109 mV higher than the standard potential. At 2000 $e^{-}\cdot Å^{-2}\cdot s^{-1}$, [$Tris^{\bullet+}$] = 7.83 mM, [Tris] = 0.08 mM, resulting in an increase of the electrochemical potential compared to the standard potential by 118 mV. Thus, we would expect a relatively small, but positive, effect from the electron beam dose on the electrochemical potential of the $Tris^{\bullet+}$/Tris redox couple.

$$Tris^{\bullet+} + e^{-} \rightarrow Tris \qquad \text{(eq. 10)}$$

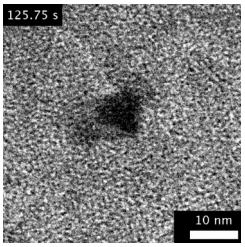


**Fig. S1. Two replicas of the time-elapsed LCTEM images (top and bottom rows) of PbSe etching trajectories**. The liquid pockets were formed by 10 mM Tris·0.5$H_2SO_4$ (400 $e^{-}\cdot Å^{-2}\cdot s^{-1}$). The results demonstrate that the etching of PbSe nanocubes was observed under this condition. The images were obtained from Movie S8.

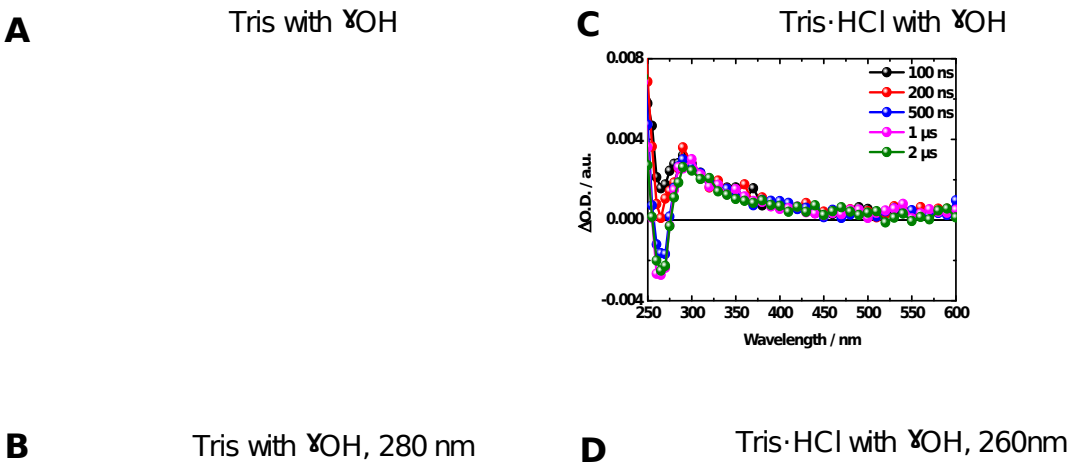


**Fig. S2. Pulse radiolysis results of Tris and Tris·HCl in $N_2O$ saturated $H_2O$. (A)** Pulse radiolysis transient absorption spectra of $2x10^{-3}$ mol·$L^{-1}$ Tris in $N_2O$ saturated $H_2O$ irradiated with electron pulses (15 ns fwhm) at a dose of 85 Gy per pulse at different time delays. **(B)** Corresponding time-dependent absorbance at 280 nm. **(C)** Pulse radiolysis transient absorption spectra of $1x10^{-3}$ mol· $L^{-1}$ Tris·HCl in $N_2O$ saturated $H_2O$ irradiated with electron pulses (15 ns fwhm) at a dose of 85 Gy per pulse at different time delays. **(D)** Corresponding time-dependent absorbance at 260 nm.

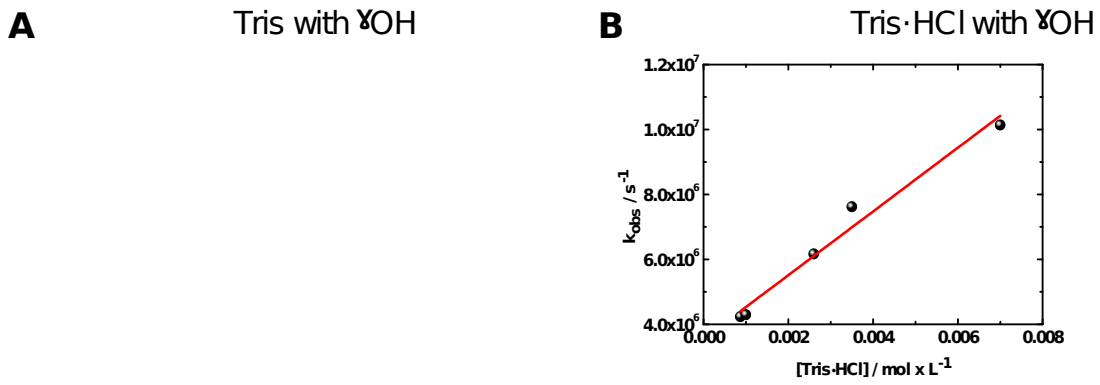


985 **Fig. S3. Plots of the pseudo-first order rate constants measured from the pulse radiolysis**
986 **experiments performed at various concentrations of Tris or Tris·HCl. (A)** Plot of the pseudo-
987 first order rate constants taken from the exponential fit of the time-dependent absorbance profile
988 measured at 280 nm vs. the Tris concentration. **(B)** Plot of the pseudo-first order rate constants
989 taken from the exponential fit of the time-dependent absorbance profile at 260 nm vs. the Tris·HCl
990 concentration.
991

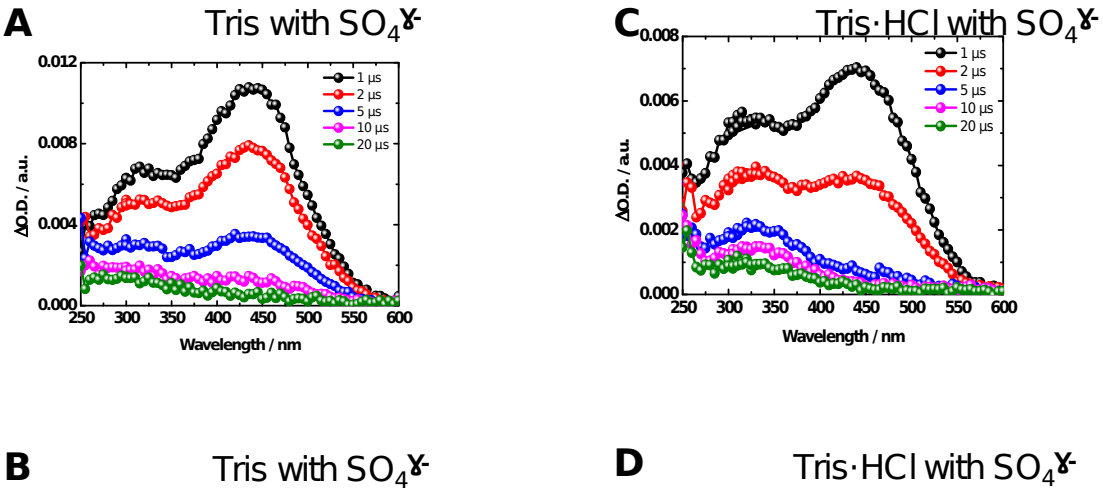


**Fig. S4. Pulse radiolysis results of Tris and Tris·HCl in $N_2$ saturated $H_2O$ containing 5 x $10^{-2}$ M $K_2S_2O_8$ and 5 vol% *t*-BuOH. (A)** Pulse radiolysis transient absorption spectrum of 2x$10^{-3}$ mol·$L^{-1}$ Tris in $N_2$ saturated $H_2O$ containing 5 x $10^{-2}$ M $K_2S_2O_8$ and 5 vol% *t*-BuOH irradiated with electron pulses (15 ns fwhm) at a dose of 30 Gy per pulse at different time delays. **(B)** Corresponding time-dependent absorbance profile of Tris at 300 nm (black) and 435 nm (red). **(C)** Pulse radiolysis transient absorption spectrum of 1x$10^{-3}$ mol·$L^{-1}$ Tris·HCl in $N_2$ saturated $H_2O$ containing 5 x $10^{-2}$ M $K_2S_2O_8$ and 5 vol% *t*-BuOH, irradiated with electron pulses (15 ns fwhm) with a dose of 30 Gy per pulse at different time delays. **(D)** Corresponding time-dependent absorbance profile of Tris·HCl at 300 nm (black) and 435 nm (red).

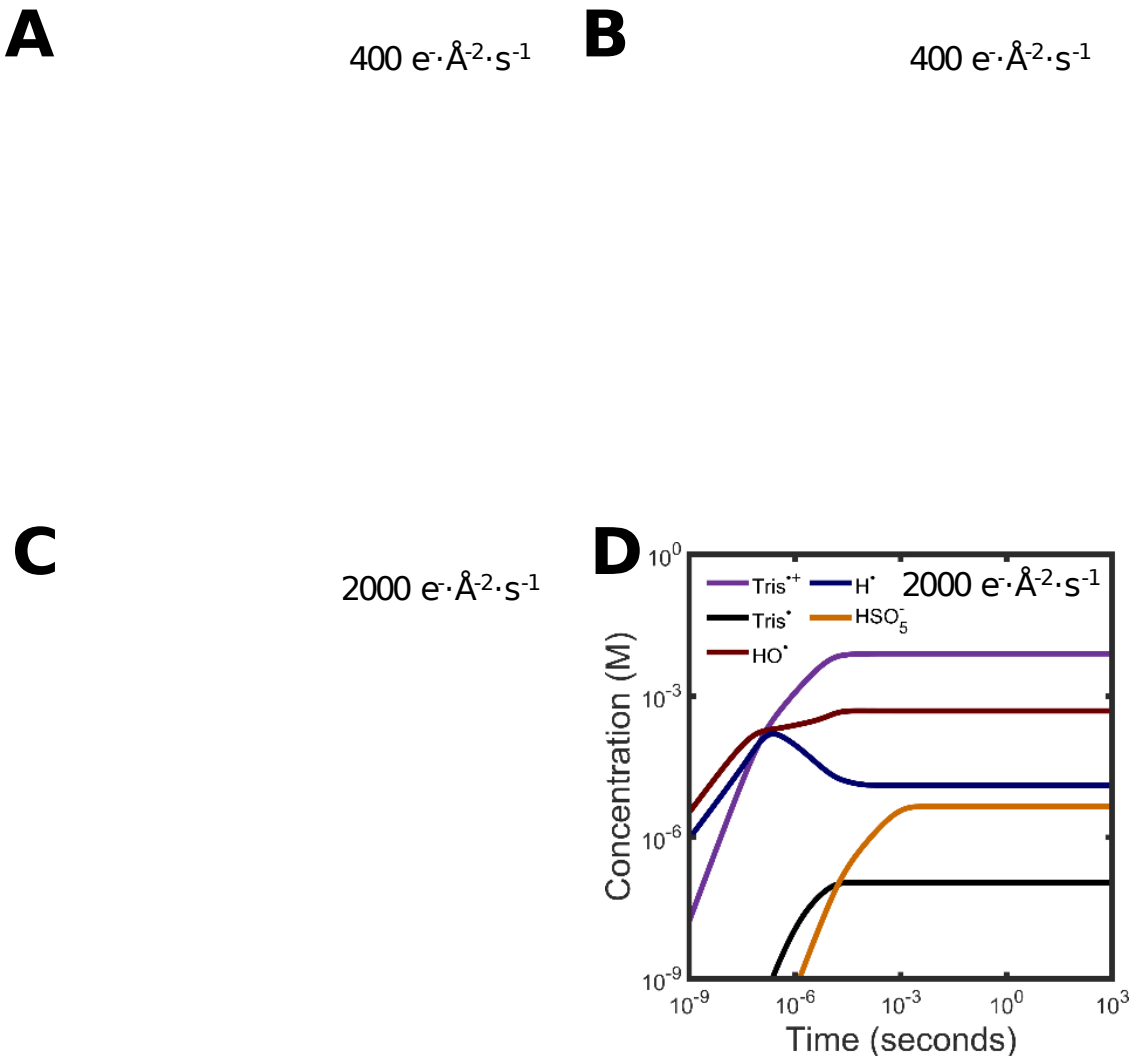


**Fig. S5. Results from the chemical network model.** Concentrations of redox species generated from radiolysis over time at an electron fluence of 400 $e^{-}\cdot Å^{-2}\cdot s^{-1}$ for **(A)** 10 mM Tris•HCl, and **(B)** 10 mM Tris•0.5($H_2SO_4$). Concentrations of radiolysis species over time at an electron fluence of 2000 $e^{-}\cdot Å^{-2}\cdot s^{-1}$ for **(C)** 10 mM Tris•HCl, and **(D)** 10 mM Tris•0.5($H_2SO_4$). The initial pH was set as pH = 5.0 for 10 mM Tris•HCl and 10 mM Tris•0.5($H_2SO_4$) solutions (Table S4).

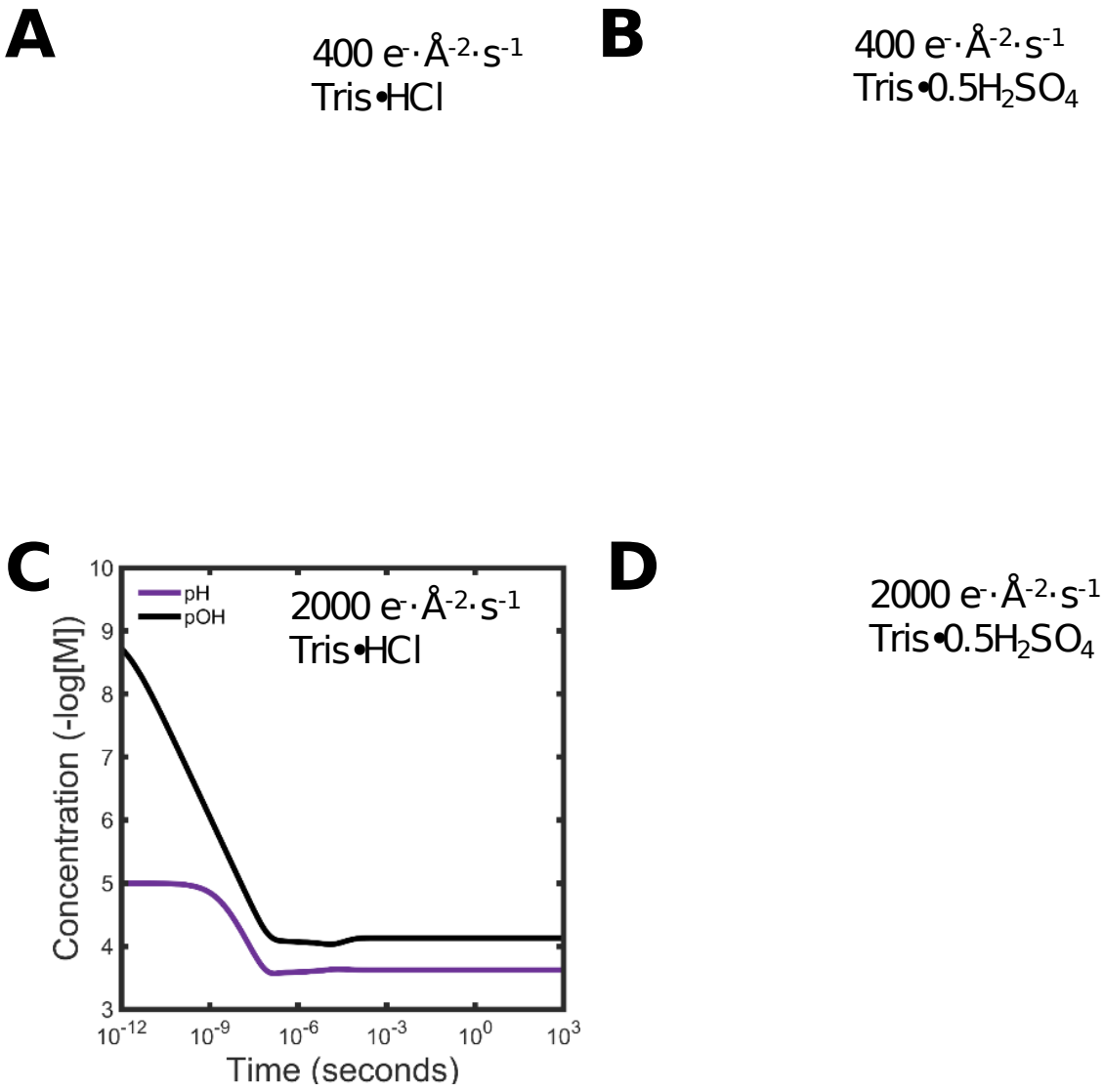


**Fig. S6. Simulated concentrations of $H^+$ and $OH^-$ over time at an electron fluence of 400 $e^-·Å^{-2}·s^{-1}$.** The results are for **(A)** 10 mM Tris•HCl, and **(B)** 10 mM Tris•0.5($H_2SO_4$). Concentrations of $H^+$ and $OH^-$ over time at an electron fluence of 2000 $e^-·Å^{-2}·s^{-1}$ for **(C)** 10 mM Tris•HCl, and **(D)** 10 mM Tris•0.5($H_2SO_4$). The initial pH was set as pH = 5.0 for 10 mM Tris•HCl and 10 mM Tris•0.5($H_2SO_4$) solutions (Table S4).

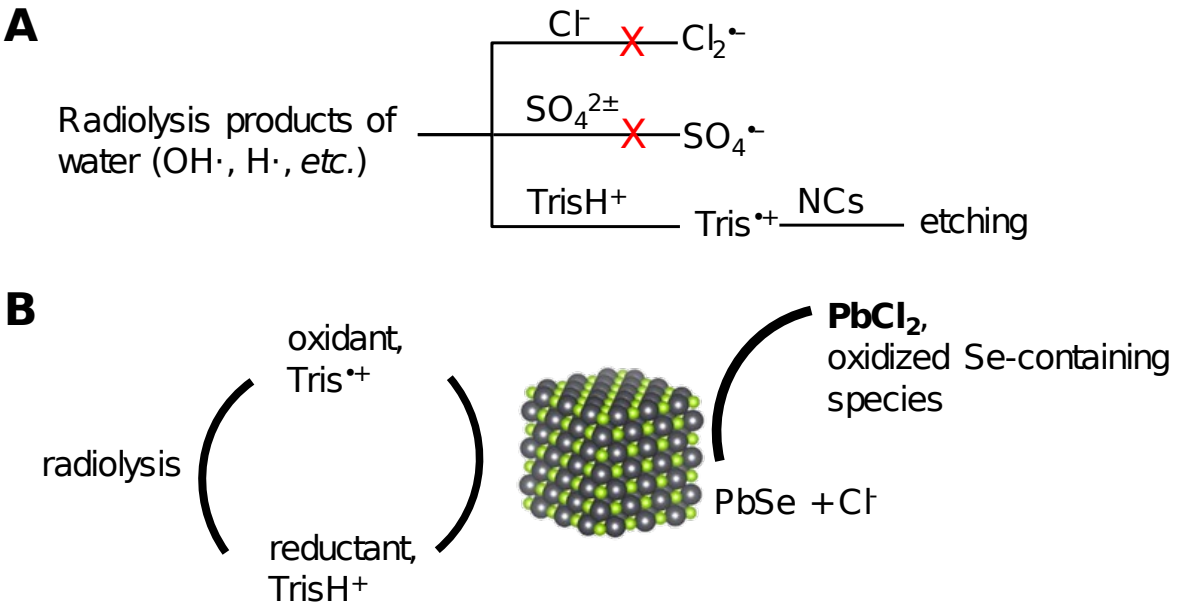


**Fig. S7. Proposed etching mechanisms. (A)** Radiolysis of Tris·HCl or Tris·0.5$H_2SO_4$ solution generates $Tris^{\bullet+}$ radicals that is proposed as the species responsible for the etching of the metal selenide nanocrystals. **(B)** The proposed reaction mechanism for the radiolysis-induced redox etching of PbSe nanocrystals in the aqueous solution of Tris·HCl.

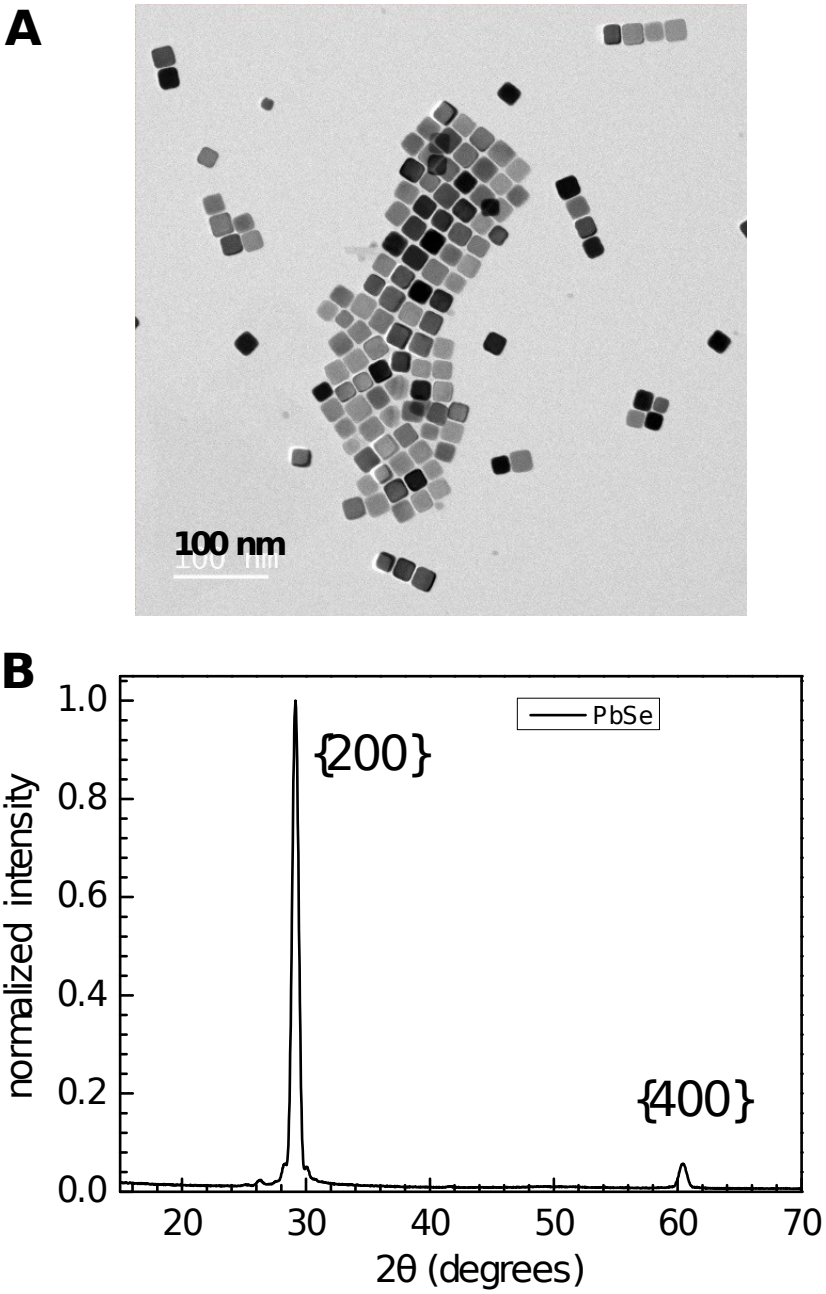


**Fig. S8. Static characterization of PbSe nanocubes used for this study.** TEM **(A)** and XRD **(B)** results show that the surface terminations are largely dominated by {100} facets.

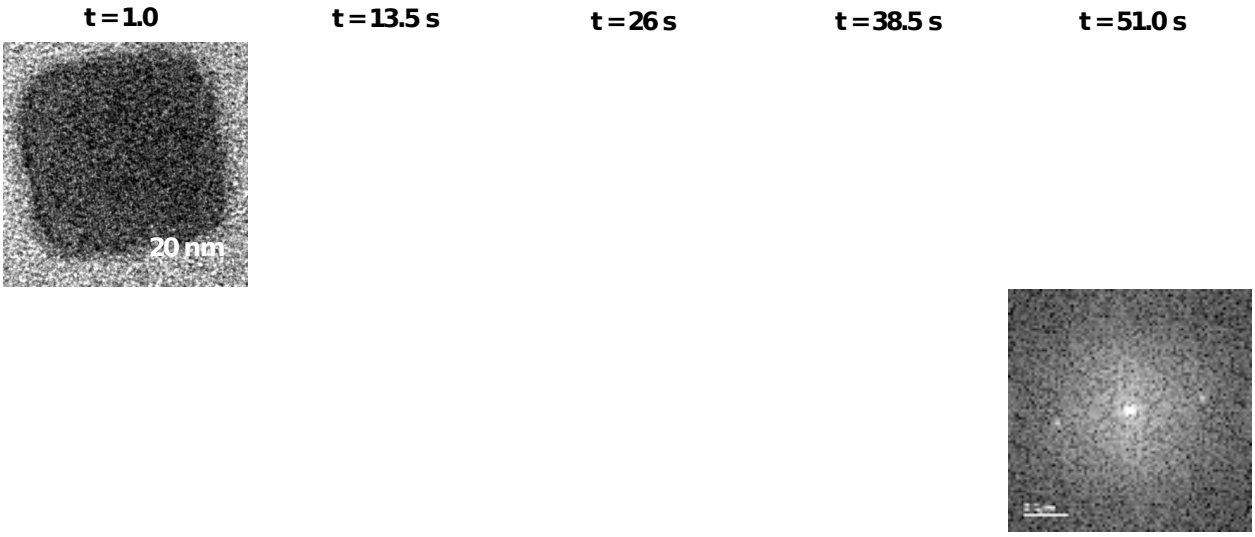


**Fig. S9. Spatial Fourier analysis of PbSe etching trajectories**. The view is along the $\langle 001 \rangle$ zone axis, and results show that the orientation of the $\{200\}$ planes maintain constant during the etching process.

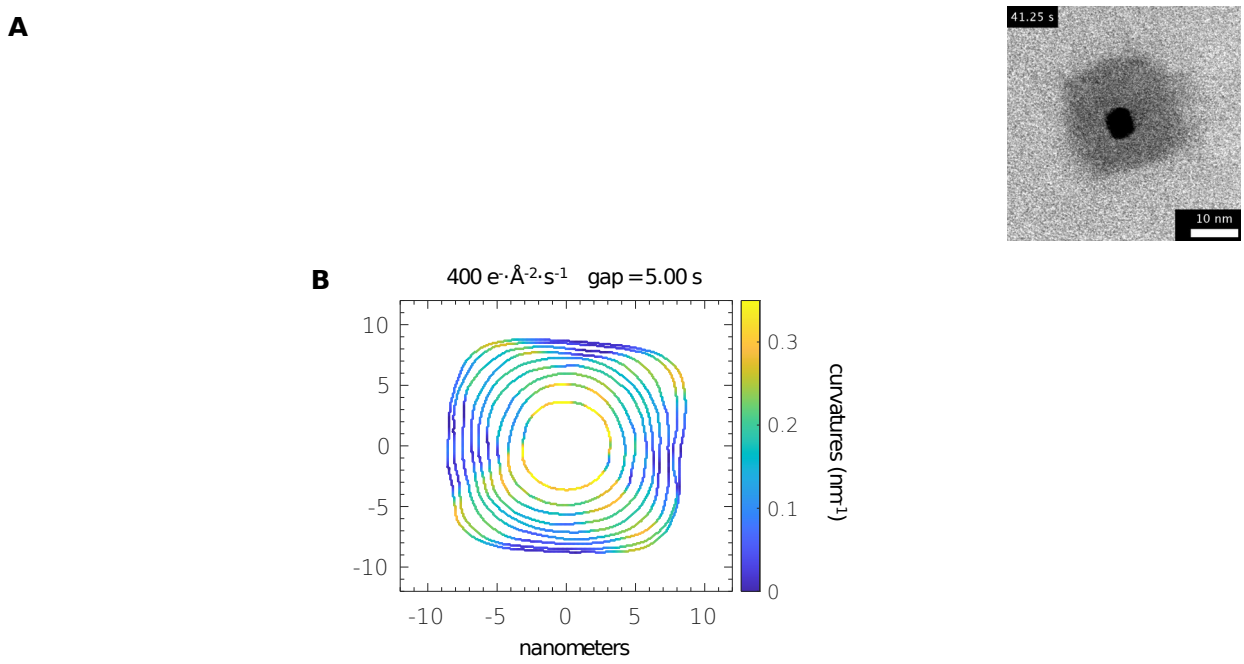


**Fig. S10. Replica of the etching trajectory of a PbSe nanocube recorded at 400 $e^{-}\cdot Å^{-2}\cdot s^{-1}$. (A)** The time-elapsed LCTEM images obtained from Movie S1. **(B)** The evolution of outlines.

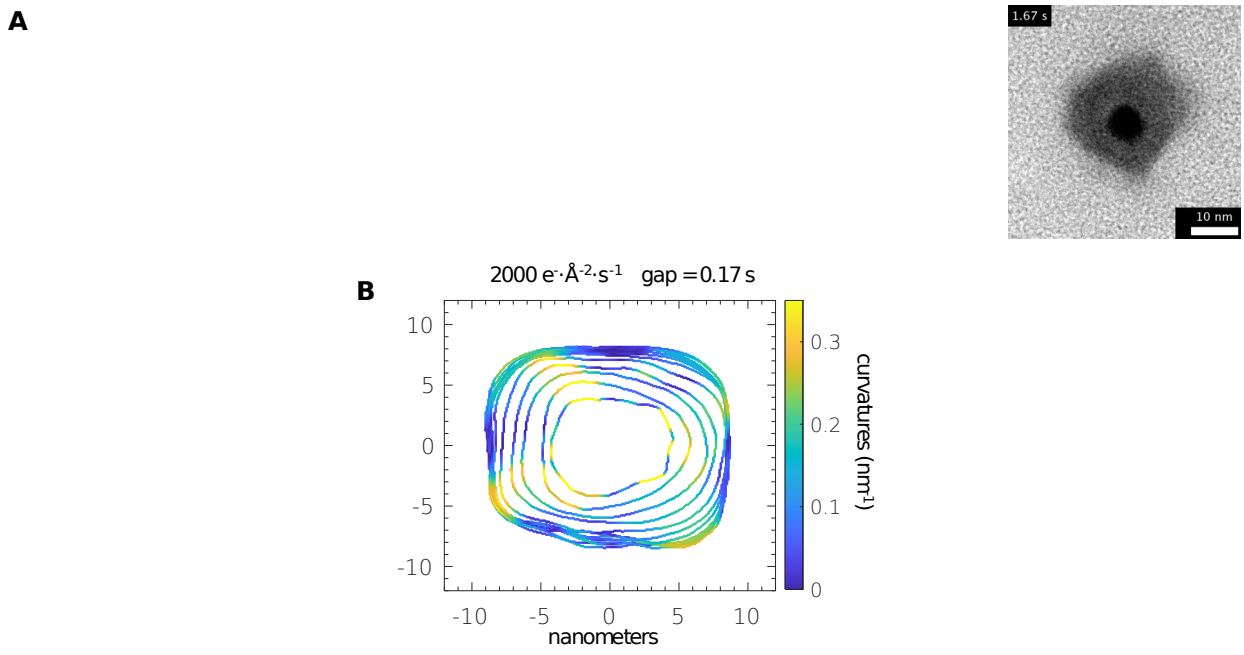


**Fig. S11. Replica of the etching trajectory of a PbSe nanocube recorded at 2000 $e^{-}\cdot Å^{-2}\cdot s^{-1}$. (A)** The time-elapsed LCTEM images obtained from Movie S2. **(B)** The evolution of outlines.

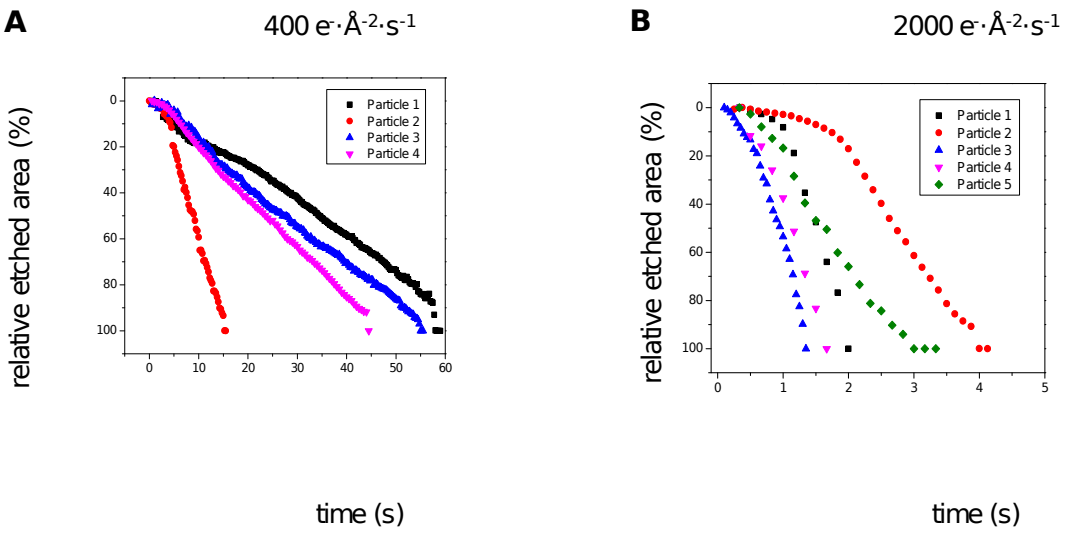


**Fig. S12. The plots of the relative etched area versus time for individual PbSe nanocrystals.** The results were obtained at 400 $e^{-}\cdot Å^{-2}\cdot s^{-1}$ **(A)** and 2000 $e^{-}\cdot Å^{-2}\cdot s^{-1}$ **(B)**.

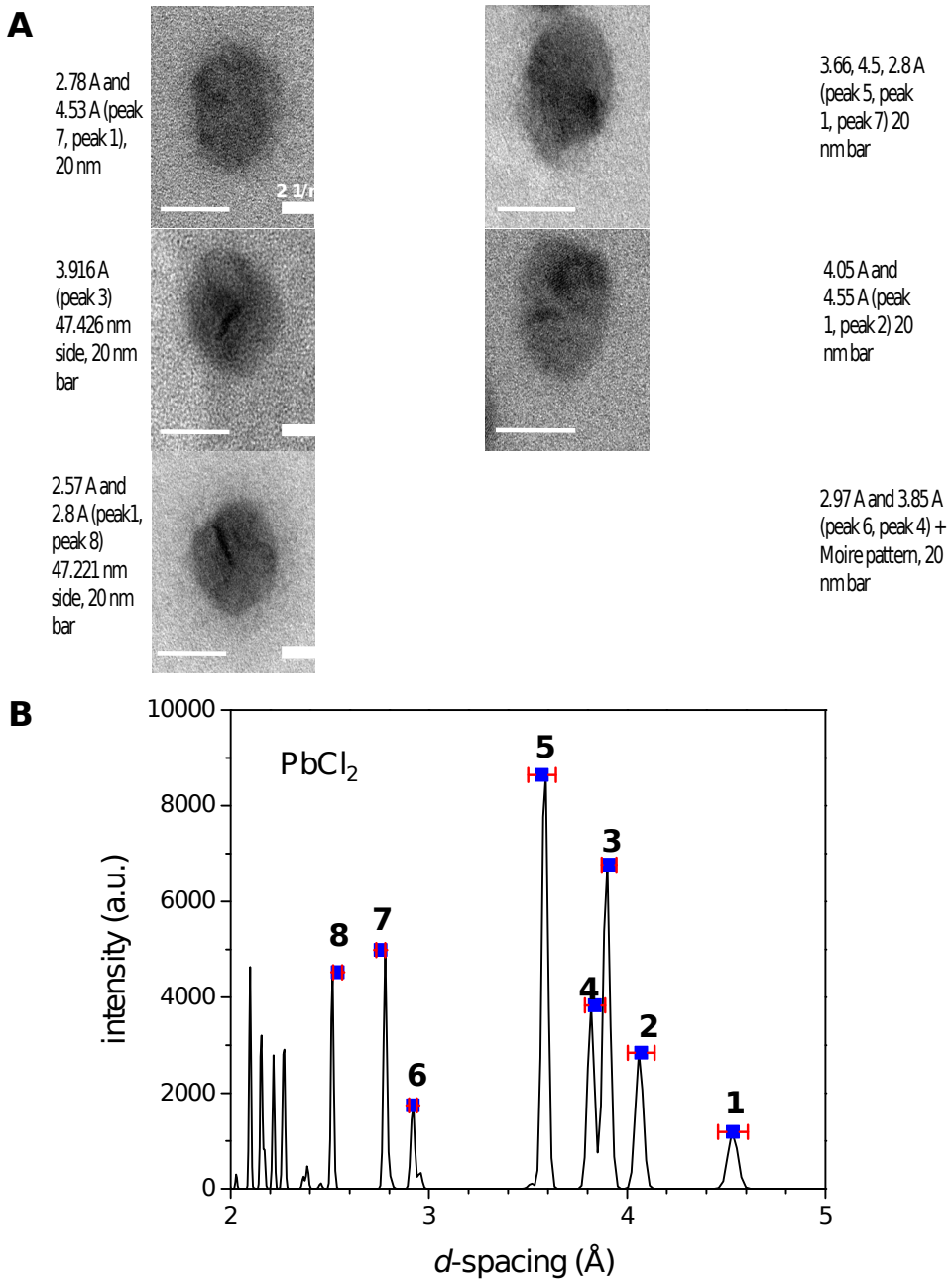


**Fig. S13. Spatial Fourier analysis of the product formed following the complete etching of PbSe nanocubes. (A)** The TEM images (scale bar = 20 nm) were collected from different etching trajectories. The Fourier transform is shown on the right side of each TEM image. A set of *d*-spacings, numbered 1-8, can be identified. **(B)** The set of the eight *d*-spacings is shown to match the XRD pattern of $PbCl_2$ in ICSD database (ID# 202130). Exact values of the *d*-spacings and the corresponding crystal planes are listed in Table S1.

**A** CdSe rods with {□□□□} lateral termination

**B** CdSe rods with {□□□□} lateral termination

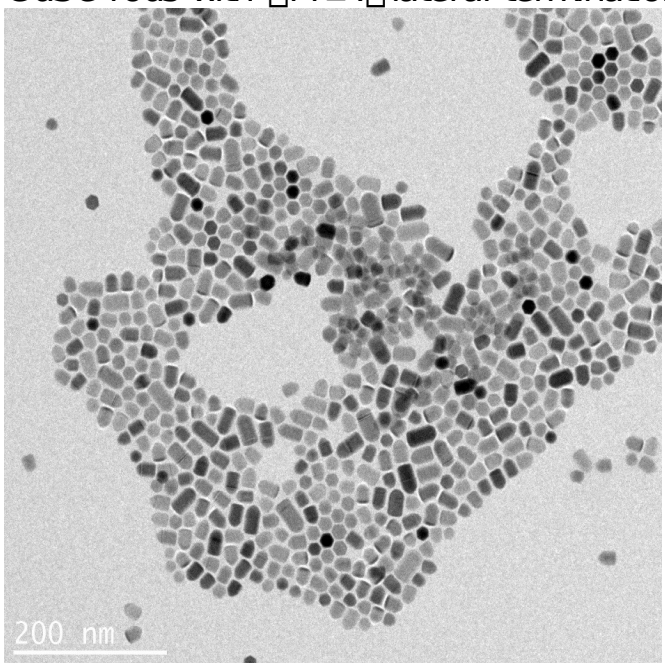


**Fig. S14. TEM images of the CdSe nanorods.** The nanorods were synthesized with two different prismatic terminations, $\{\acute{1}\,100\}$ facets **(A)** and $\{11\acute{2}\,0\}$ facets **(B)**.

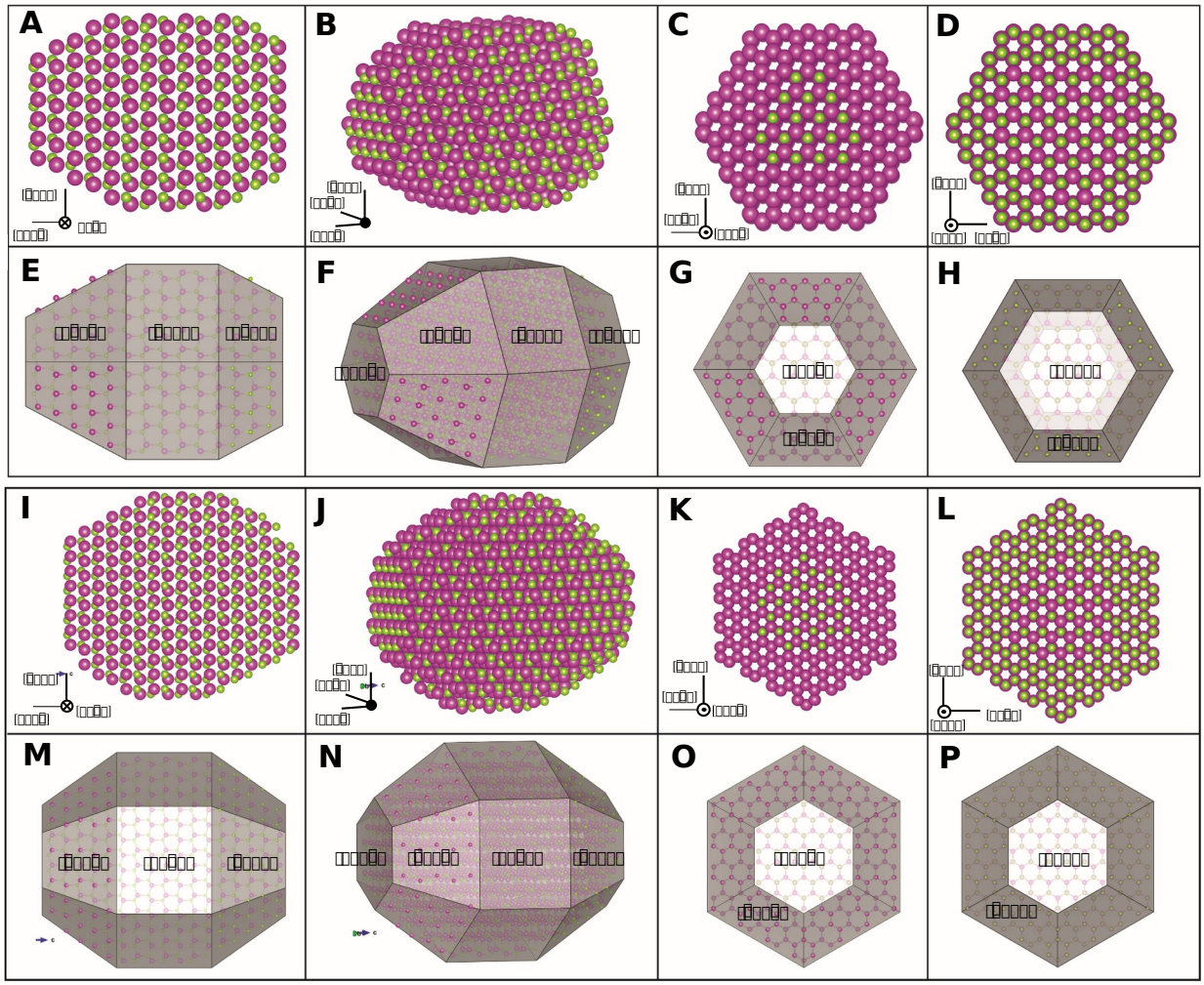


**Fig. S15. 3D atomistic models of wurtzite CdSe nanocrystals with $\{\acute{1}100\}$ prismatic facets (A-H) and $\{11\acute{2}0\}$ prismatic facets (I-P) viewed along different directions.** Pink atoms are Cd, and green atoms are Se. Panels E, F, G, and H display labeled facets associated with the models in panels A, B, C, and D, respectively. Panels C and G show that the $(000\acute{1})$ facet is terminated with Se (green) atoms, and the $\{1\acute{1}0\acute{1}\}$ facets are terminated with Cd (red) atoms. Panels D and H show that the $(0001)$ facet is terminated with Cd (red) atoms, and the $\{1\acute{1}01\}$ facets are terminated with Se (green) atoms. Similarly, panels M, N, O, and P display labeled facets associated with the models in panels I, J, K, and L, respectively. Panels K and L show that $\{\acute{2}11\acute{2}\}$ facets are terminated with Cd (red) atoms, and $\{\acute{2}112\}$ facets are terminated with Se (green) atoms.

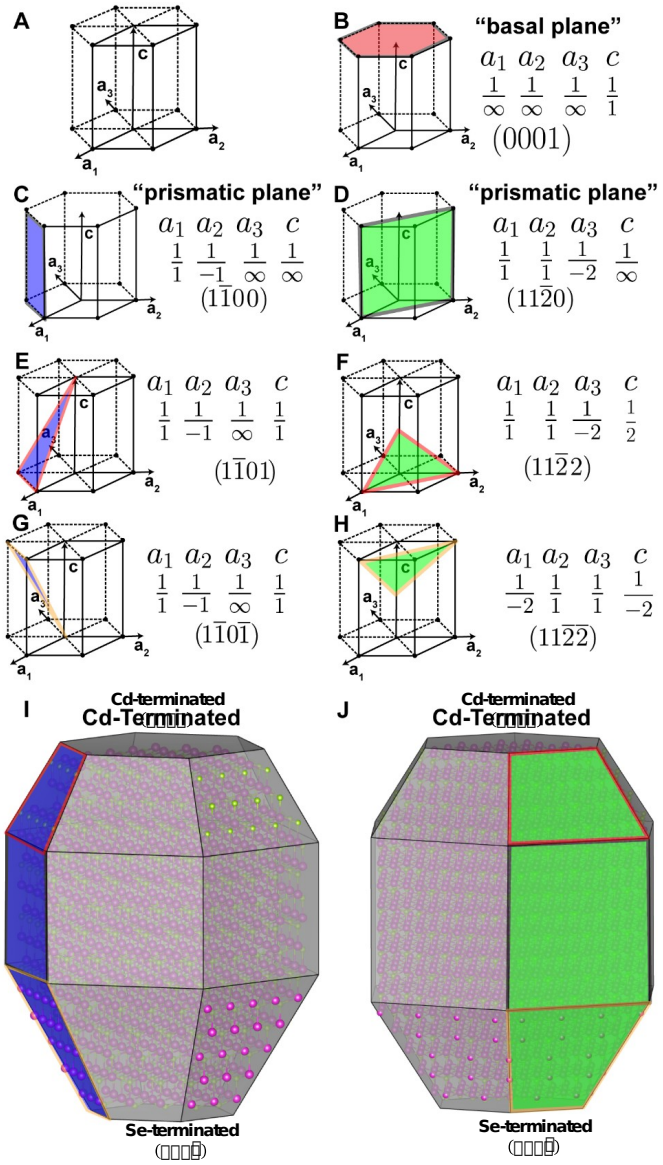


**Fig. S16. The Miller-Bravais notation system for hexagonal crystals and the representation of facets typically observed in wurtzite CdSe nanorods.** In the Miller-Bravais system shown in panel **A**, 4 unit vectors, $a_1, a_2, a_3$, and $c$, are used to define planes by their fractional intercept with the unit vectors. For example, a basal plane (red) illustrated in panel **B** only intersects the $c$-axis, resulting in the (0001) delineation for the Cd-terminated basal plane. Conversely the Se-terminated basal plane of the crystal has the $\left(000\,\acute{1}\right)$ delineation. The prismatic $\{\acute{1}\,100\}$ facets **(C)** and $\{11\acute{2}\,0\}$ facets **(D)** are the planes which form the sides of the nanorods. Joining the prismatic and basal planes are a set of pyramidal planes (**E-H**) which result in the truncated shape of the nanorods. Importantly the pyramidal planes which join their respective basal planes have the opposite termination as the basal plane. For example, the (0001) is Cd-terminated but the $\left(1\,\acute{1}\,01\right)$ and the $\left(11\acute{2}\,2\right)$ are Se-terminated. 3D renderings of wurtzite crystallites terminated with $\left\{1\,\acute{1}\,00\right\}$ and $\left\{11\acute{2}\,0\right\}$ prismatic planes are shown in panels **I** and **J**, respectively. The blue planes in panel I correspond to the colored planes in panels C, E, and G. The green planes in panel J correspond to the colored planes in panels D, F, and H.

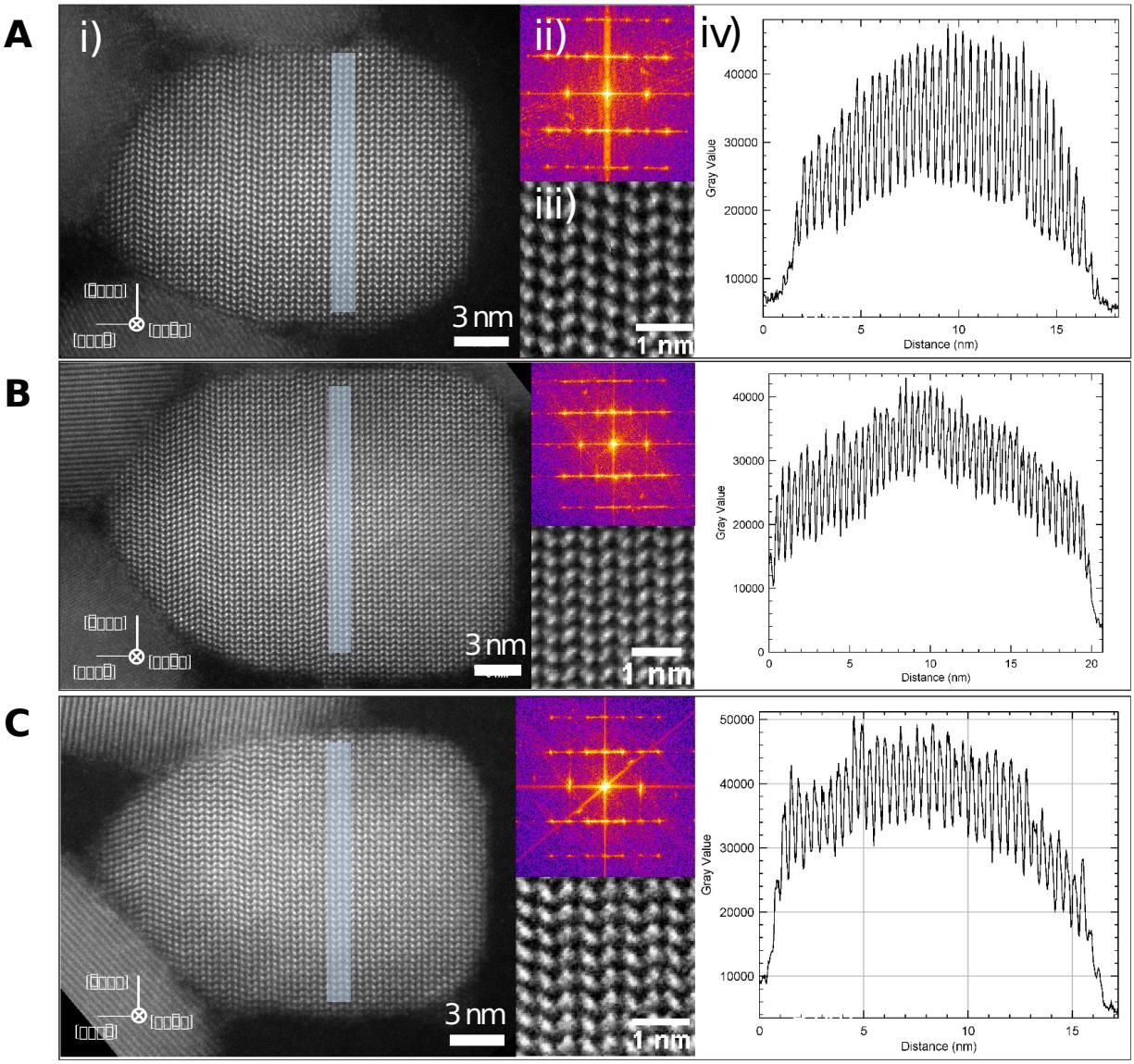


**Fig. S17. AC-HAADF-STEM images of {$\acute{1}100$} terminated CdSe nanorods viewed down the [$11\acute{2}0$] zone axis showing the orientation of the lattice relative to the shape of the nanorods.** The tip is Se-terminated and the flat bottom is Cd-terminated. **i)** shows AC-HAADF-STEM images, **ii)** shows the Fourier transform of the image, **iii)** shows a magnified AC-HAADF-STEM image, and **iv)** shows an intensity profile across the particle performed within the shaded area in (i). The intensity profile shows a peak in the middle which corresponds to a vertex of a projected hexagon. Panels **(A)-(C)** are three replicas of the HRTEM analysis.

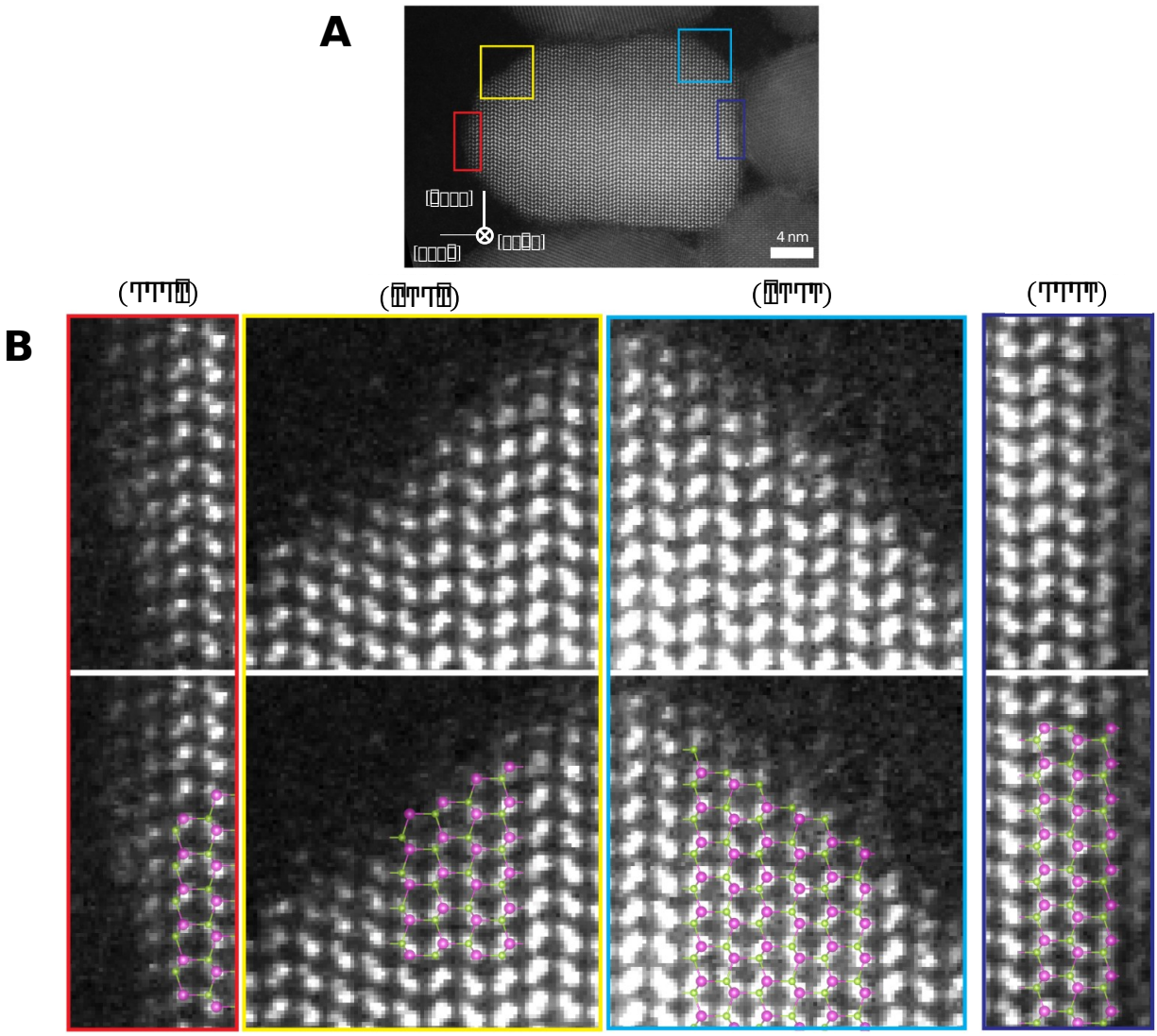


**Fig. S18. High resolution HAADF-STEM analysis of {$\bar{1}$ 100} CdSe rods showing the termination of different polar facets including the corners, viewed down the [11$\bar{2}$0] zone axis.** The regions analyzed are indicated by color-coded rectangles shown in panel **A**. In panel **B**, the atomistic models are overlaid onto the images to show that $(000\bar{1})$ and $(\bar{1}101)$ facets are Se-terminated; $(0001)$ and $(\bar{1}10\bar{1})$ facets are Cd-terminated. Pink dots indicate Cd, and green dots indicate Se.

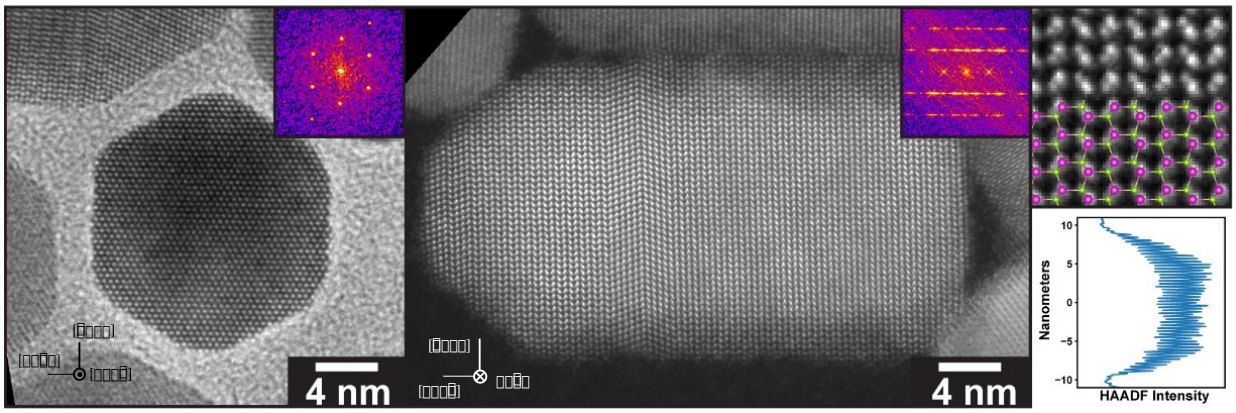


**Fig. S19. Representative TEM images of wurtzite CdSe nanocrystals terminated with {11$\acute{2}$0} facets viewed along the *c*-axis (hexagon disk projection) and the [11$\acute{2}$0] zone axis (nanorod projection).** Same as the case for CdSe nanocrystals with {$\acute{1}$100} prismatic terminations, the AC-HAADF-STEM image of the {11$\acute{2}$0} nanorod shows that the tip of rod is Se-terminated while the bottom of the rod is Cd-terminated. The intensity profile across the particle is performed within the shaded area. The intensity profile shows a plateau in the center which corresponds to a prismatic face of a projected hexagon.

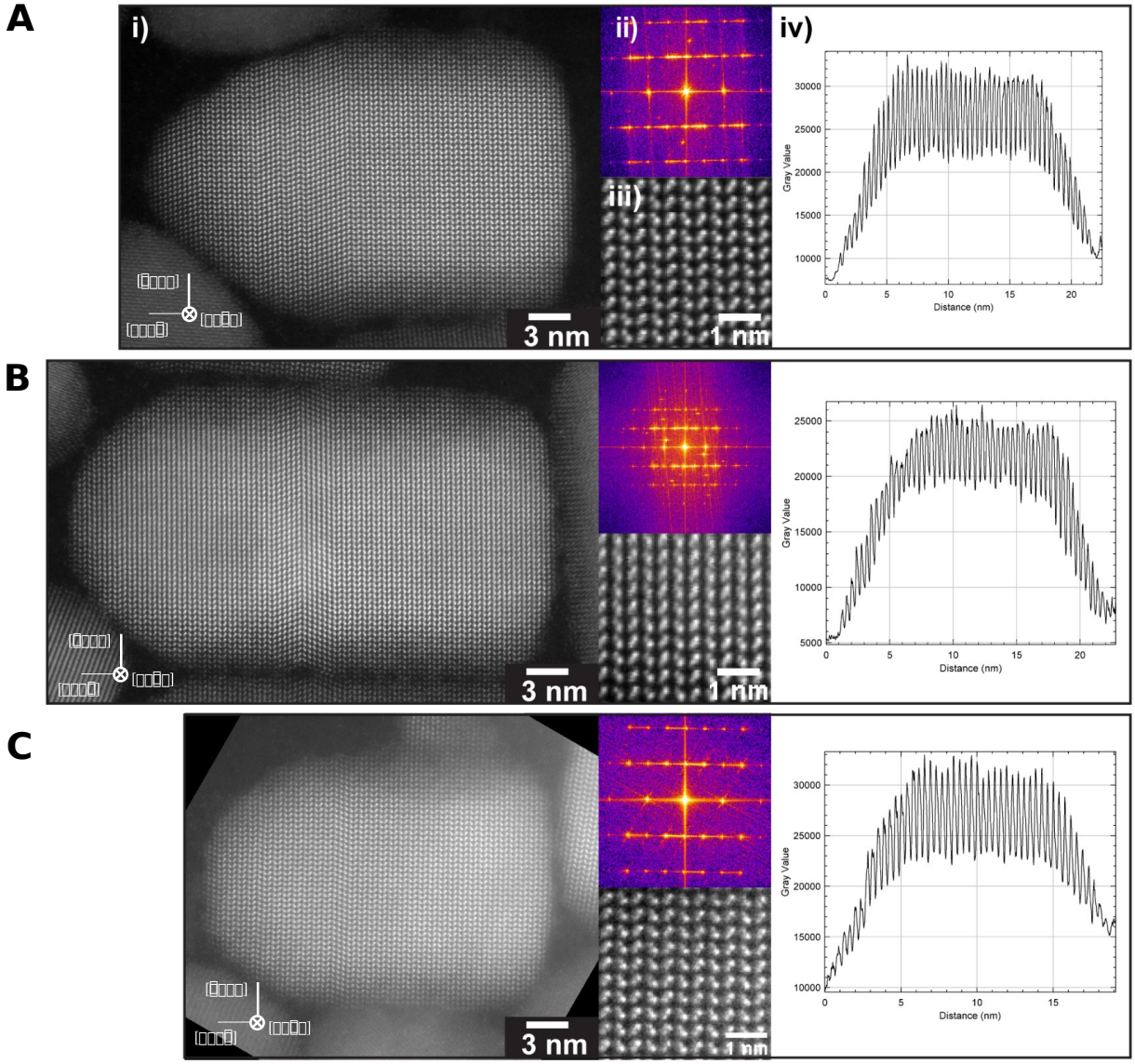


**Fig. S20. AC-HAADF-STEM images of {11$\acute{2}$0} terminated CdSe nanorods viewed along the [11$\acute{2}$0] zone axis showing the orientation of the lattice relative to the shape of the nanorods.** The tip is Se-terminated and the flat bottom is Cd-terminated. **i)** shows AC-HAADF-STEM images, **ii)** shows the Fourier transform of the image, **iii)** shows a magnified AC-HAADF-STEM image, and **iv)** shows an intensity profile across the particle performed within the shaded area. The intensity profile shows a plateau which corresponds to a prismatic face of a projected hexagon. Panels **(A)-(C)** are three replicas of the HRTEM analysis.

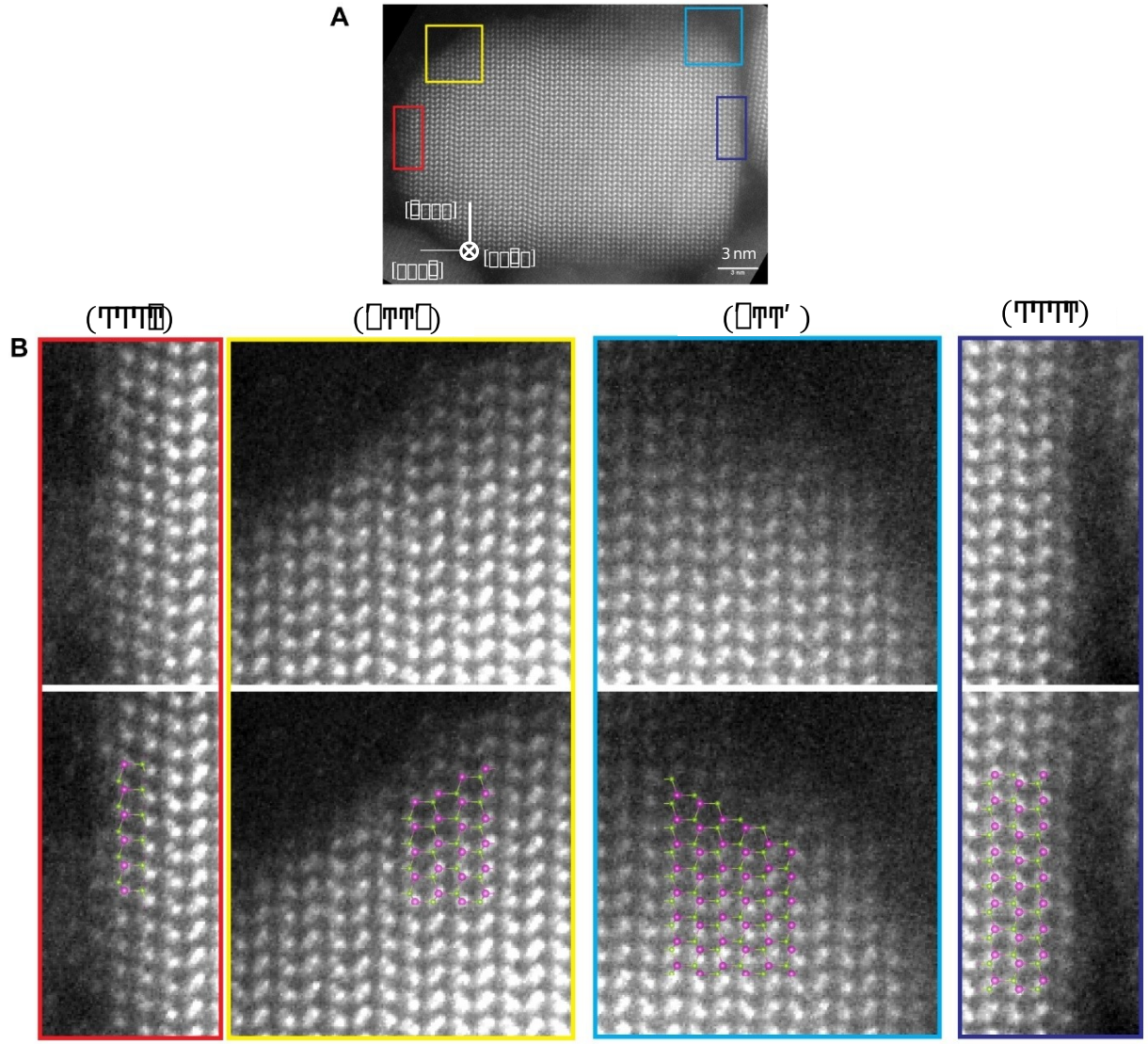


**Fig. S21. High resolution HAADF-STEM analysis of {$11\bar{2}0$} CdSe rods showing the termination of different polar facets including the corners, viewed down the [$11\bar{2}0$] zone axis.** The regions analyzed are indicated by color-coded rectangles in panel **A**. The atomistic models overlaid on the images in panel **B** show that $(000\bar{1})$ and $(\bar{2}11\bar{2})$ facets are Se-terminated; $(0001)$ and $(\bar{2}112)$ facets are Cd-terminated. Pink dots indicate Cd atoms, and green dots indicate Se atoms.

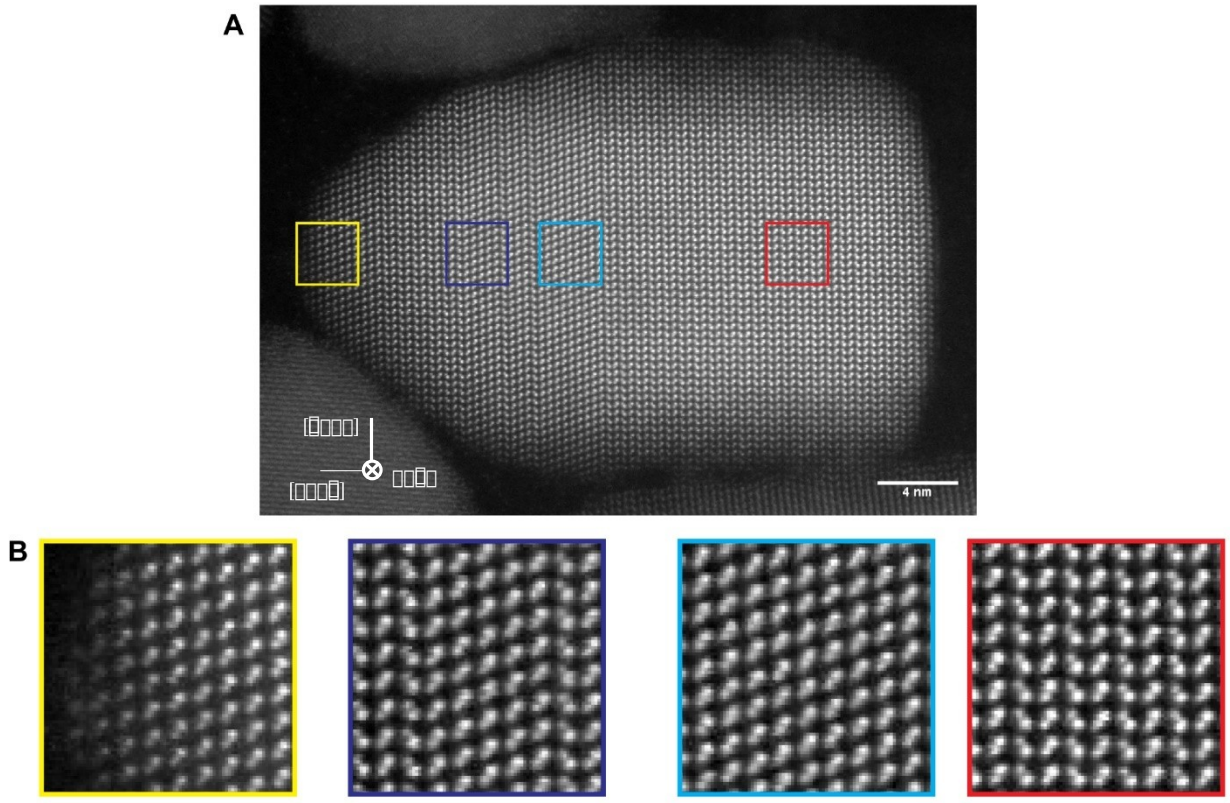


**Fig. S22. High resolution HAADF-STEM of a CdSe nanorod which shows considerable zinc blende inclusions, viewed down the [11$\acute{2}$0] zone axis.** The polarity of the wurtzite lattice is transferred to the zinc blende inclusions such that the zinc blende inclusion has no effect on the termination of facets being Cd-terminated or Se-terminated.

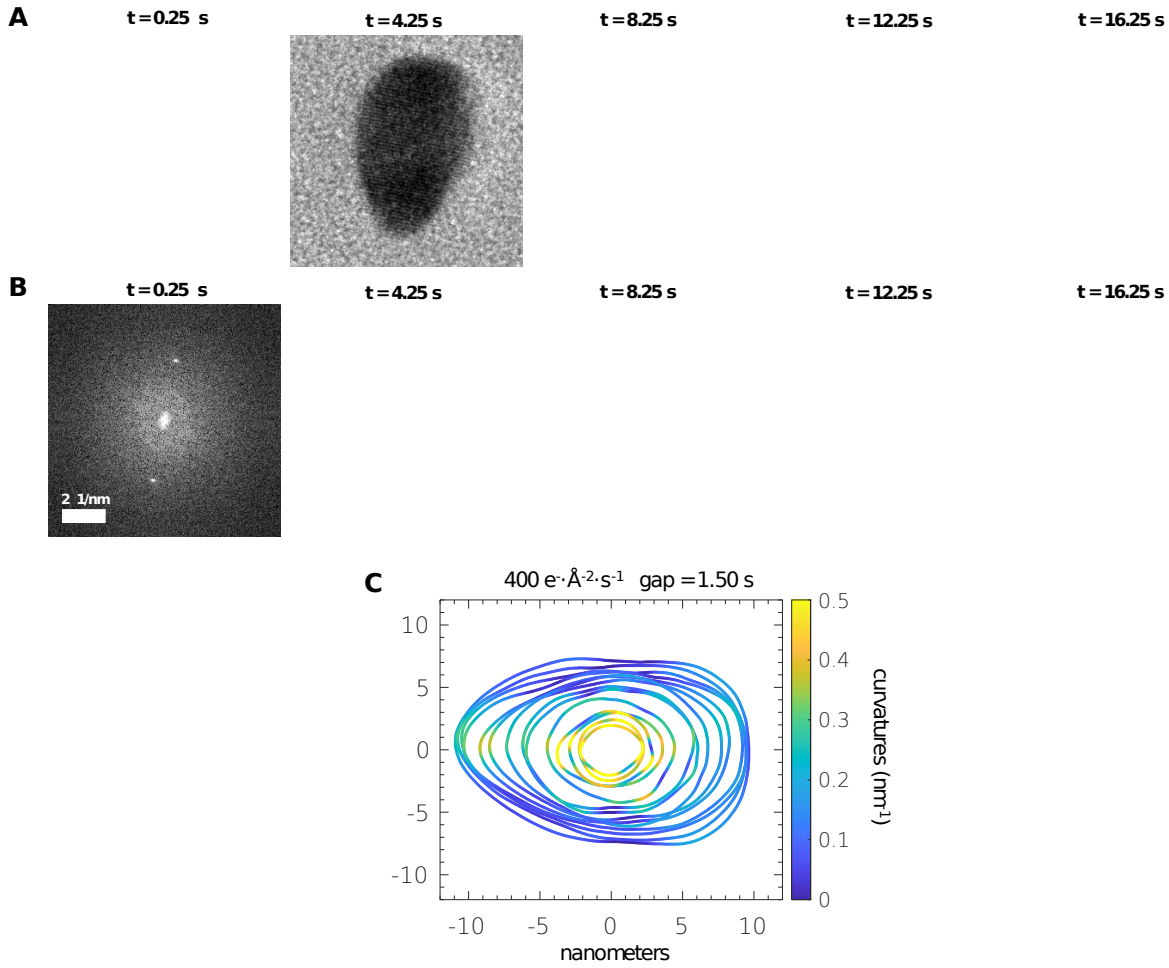


**Fig. S23. Replica of the etching trajectory of a CdSe nanorod with $\{\bar{1}100\}$ prismatic facets recorded at 400 $e^{-}\cdot Å^{-2}\cdot s^{-1}$ and viewed along the $\langle\bar{1}100\rangle$ zone axis. (A)** The time-elapsed LCTEM images obtained from Movie S3. **(B)** Spatial Fourier analysis of the CdSe etching trajectory indicates that the orientation of the $\langle 0001\rangle$crystal axis remains constant during the etching process. **(C)** The evolution of outlines.

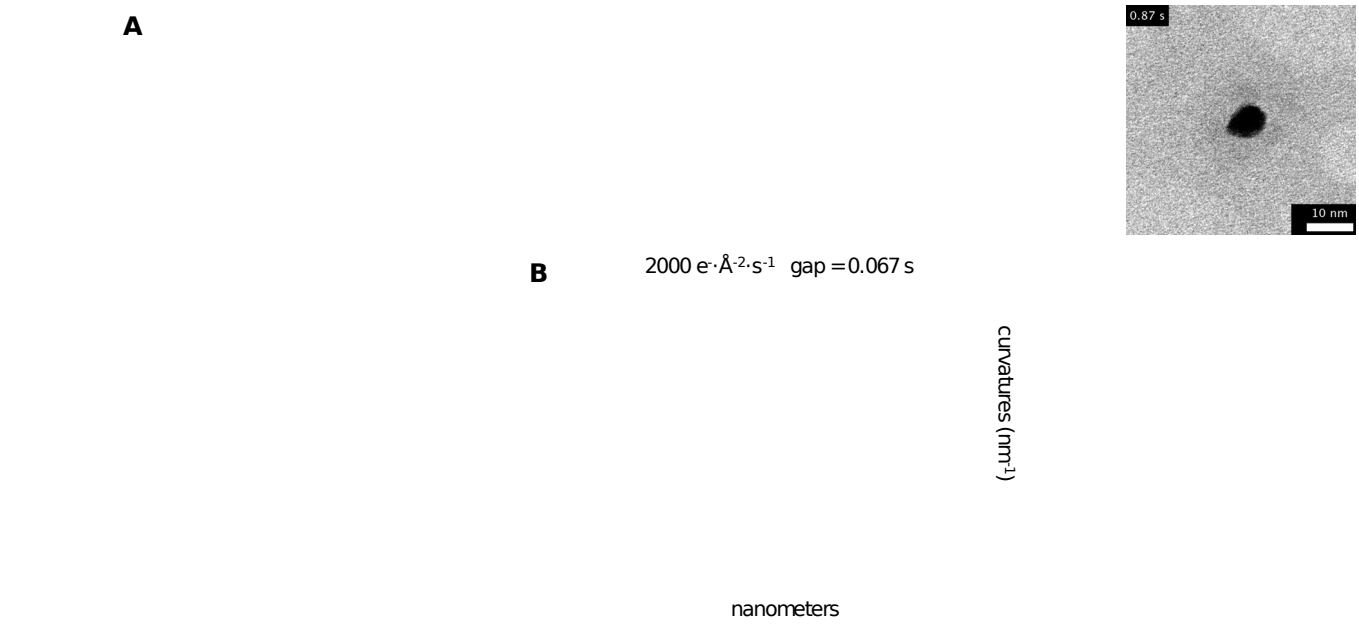


**Fig. S24. Replica of the etching trajectory of a CdSe nanorod with $\{\bar{1}100\}$ prismatic facets recorded at 2000 $e^{-}\cdot Å^{-2}\cdot s^{-1}$.** **(A)** The time-elapsed LCTEM images obtained from Movie S4. **(B)** The evolution of outlines.

**A**

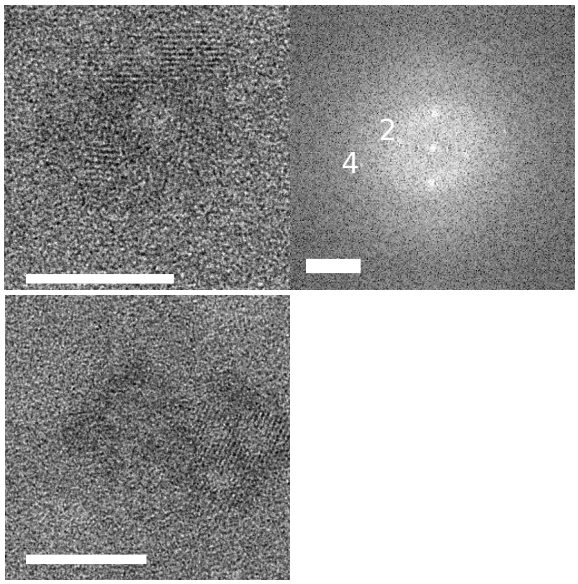


**B**

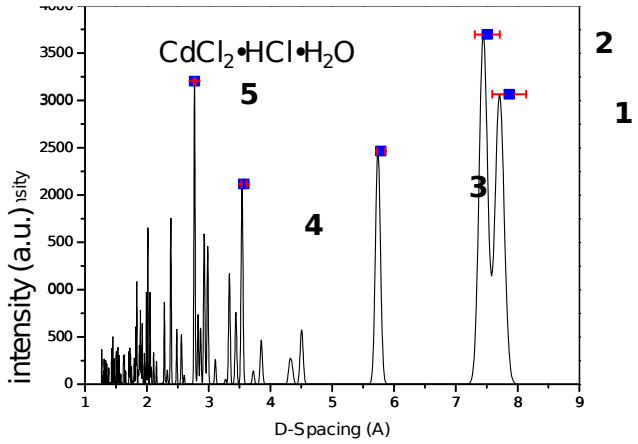


*d*-spacing (Å)

1141

**Fig. S25. Spatial Fourier analysis of the product formed following the complete etching of CdSe nanorods. (A)** The TEM images (scale bar = 20 nm) were collected from different etching trajectories. The Fourier transform is shown on the right side of each TEM image. A set of *d*-spacings, numbered 1-5, can be identified. **(B)** The set of the five *d*-spacings is shown to match the XRD pattern of $CdCl_2$•HCl•$H_2O$ in ICSD database (ID# 426115). Exact values of the *d*-spacings and the corresponding crystal planes are listed in Table S2.

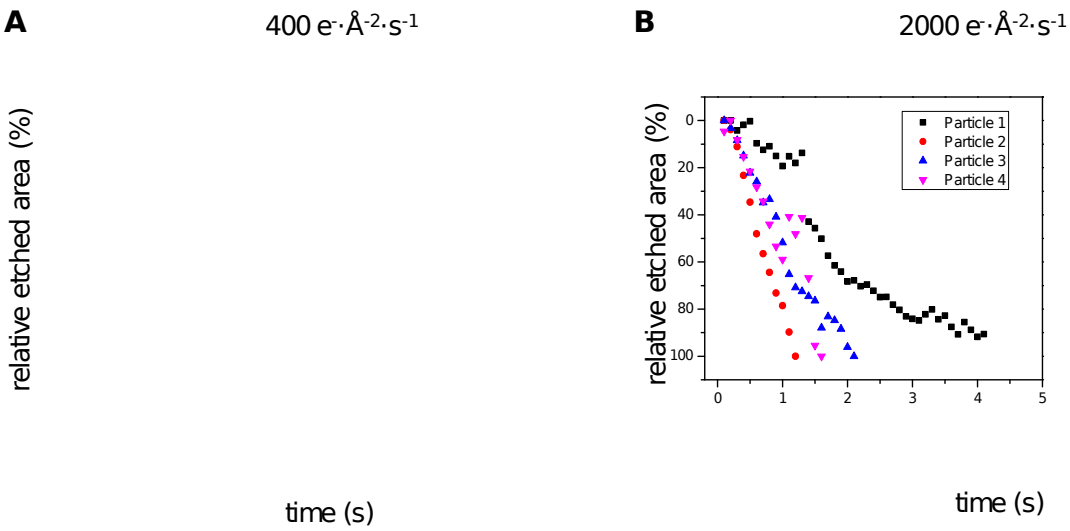


**Fig. S26. The plots of the relative etched area versus time for individual CdSe nanocrystals.** The results were obtained at 400 $e^{-}\cdot Å^{-2}\cdot s^{-1}$ **(A)** and 2000 $e^{-}\cdot Å^{-2}\cdot s^{-1}$ **(B)**.

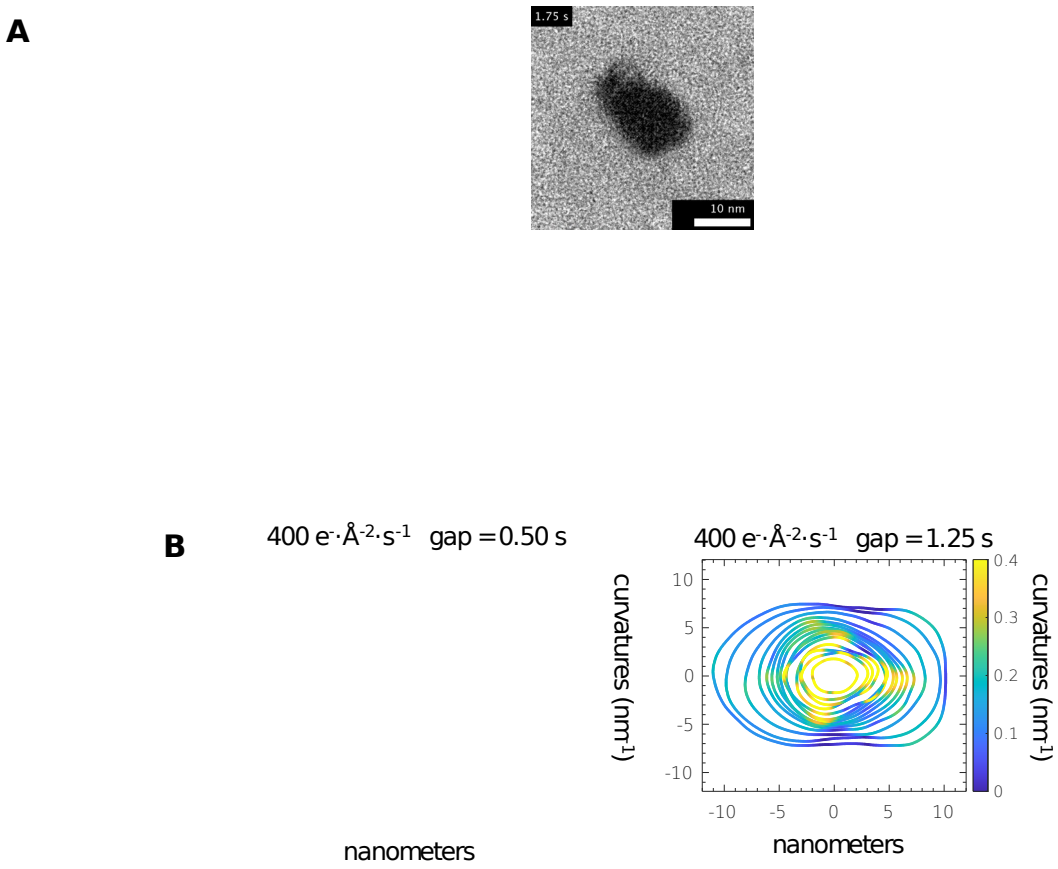


**Fig. S27. Two replicas of the etching trajectories of CdSe nanorods with $\{11\bar{2}0\}$ prismatic facets recorded at 800 $e^{-}\cdot Å^{-2}\cdot s^{-1}$. (A)** The time-elapsed LCTEM images obtained from Movie S5. **(B)** The evolution of outlines. The outlines on the left side correspond to the LCTEM images in the upper row of panel A, and the outlines on the right side correspond to the LCTEM images in the bottom row of panel A.

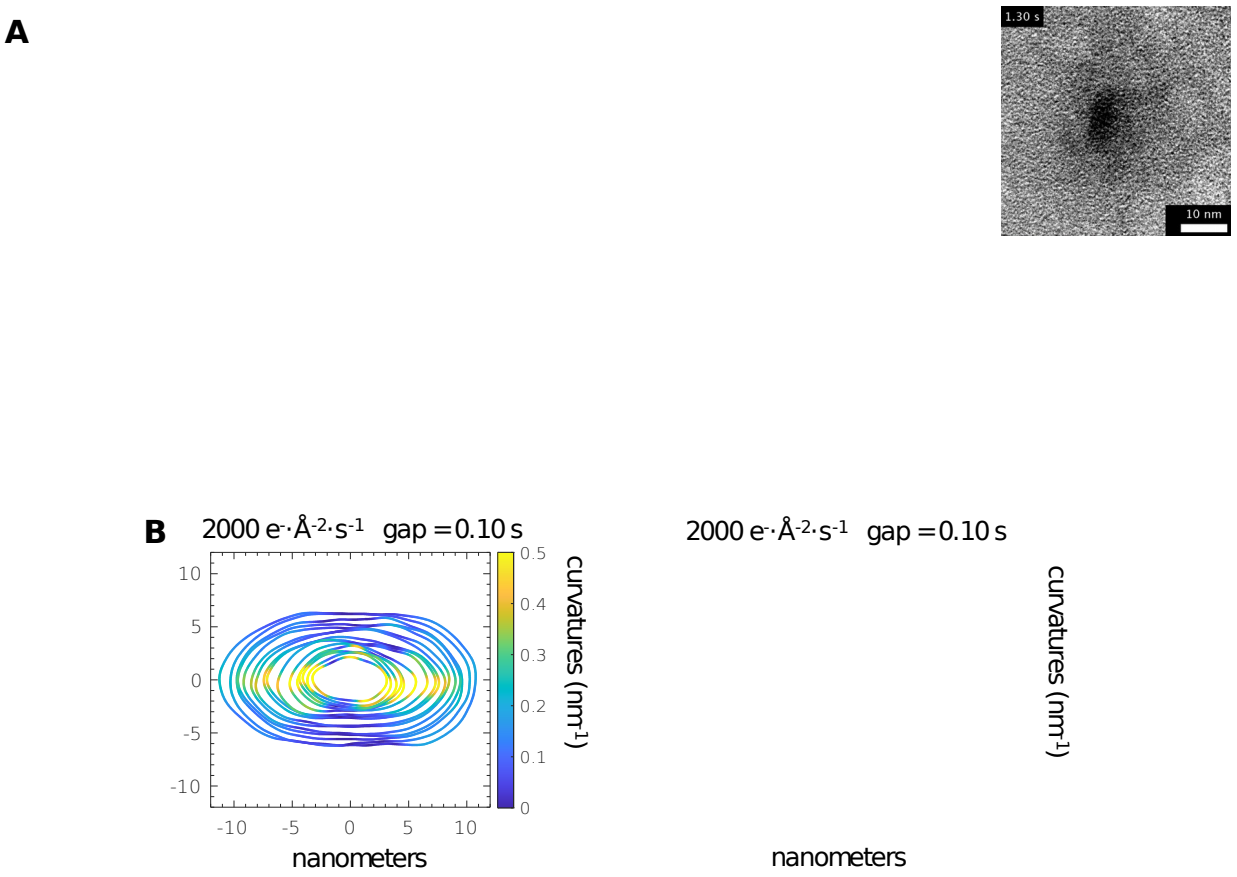


**Fig. S28. Two replicas of the etching trajectories of CdSe nanorods with $\{11\bar{2}0\}$ prismatic facets recorded at 2000 $e^{-}\cdot Å^{-2}\cdot s^{-1}$. (A)** The time-elapsed LCTEM images obtained from Movie S6. **(B)** The evolution of outlines. The outlines on the left side correspond to the LCTEM images in the upper row of panel A, and the outlines on the right side correspond to the LCTEM images in the bottom row of panel A.

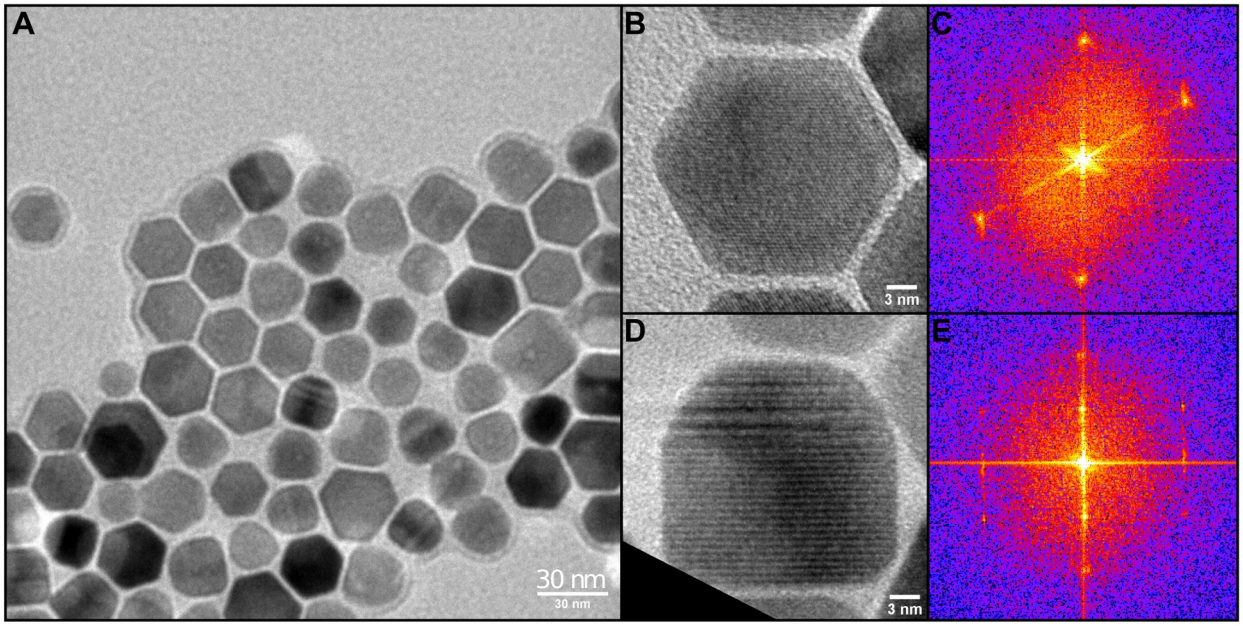


**Fig. S29. Characterization of the wurtzite CdSe nano-disk sample with $\{\bar{1}100\}$ prismatic terminations.** **(A)** Low magnification TEM, **(B)** HRTEM image viewed down the $\langle 0001 \rangle$ zone axis and **(C)** the corresponding Fourier transform, **(D)** image of a particle tilted on the side showing the low aspect ratio, and **(E)** the corresponding Fourier transform.

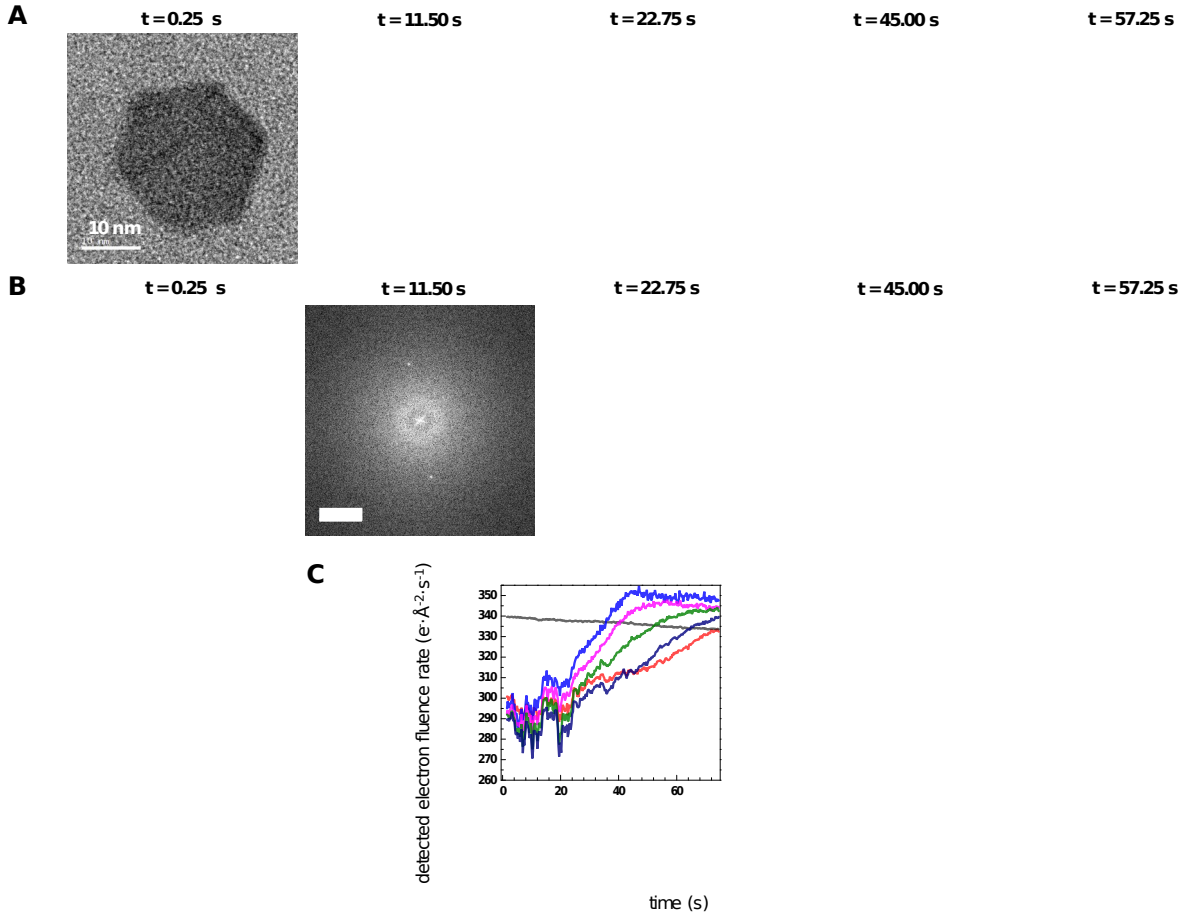


**Fig. S30. Replica of the etching trajectory of a CdSe nanodisk projected along the $\langle 0001 \rangle$ zone axis recorded at 400 $e^{-}\cdot Å^{-2}\cdot s^{-1}$.** The hexagonal prismatic facets are $\{ \acute{1}\, 100 \}$ facets. **(A)** The time-elapsed TEM images obtained from Movie S7. **(B)** Spatial Fourier analysis of the CdSe etching trajectory in indicates that the orientation of the $[ \acute{1}\, 100 ]$ crystal axis remains constant during the etching process. **(C)** The plot of the average electron fluence rates in color-coded spatial segments versus time, indicating the formation of a concave pit as etching proceeds.

| Peaks | XRD references (Å) | 2θ (degrees) | Measured *d*-spacings (Å) | Planes |
|---|---|---|---|---|
| 1 | 4.525 | 19.6 | 4.53 | {002} |
| 2 | 4.053 | 21.9 | 4.17 | {101} |
| 3 | 3.889 | 22.9 | 3.95 | {102} |
| 4 | 3.810 | 23.3 | 3.88 | {200} |
| 5 | 3.577 | 24.9 | 3.61 | {111} |
| 6 | 2.921 | 30.6 | 2.96 | {210} |
| 7 | 2.775 | 32.2 | 2.80 | {211} |
| 8 | 2.510 | 35.7 | 2.58 | {013} |

**Table S1.** The numbered *d*-spacings identified by Fourier analysis of TEM images acquired after the complete etchings of PbSe nanocubes are listed alongside the powder XRD peak positions of $PbCl_2$ in the ICSD database (ID# 202130, see also Fig. S13).

| Peaks | XRD references (Å) | 2θ (degrees) | Measured *d*-spacings (Å) | Planes |
|---|---|---|---|---|
| 1 | 7.715 | 11.47 | 7.83 | {101} |
| 2 | 5.443 | 15.89 | 5.47 | {002} |
| 3 | 5.742 | 15.43 | 5.79 | {102} |
| 4 | 3.544 | 25.15 | 3.57 | {111} |
| 5 | 2.772 | 32.29 | 2.77 | {212} |

**Table S2.** The numbered *d*-spacings identified by Fourier analysis of TEM images acquired after the complete etchings of CdSe nanorods are listed alongside the powder XRD peak positions of $CdCl_2 \bullet HCl \bullet H_2O$ in the ICSD database (ID# 426115, see also Fig. S25).

| Reaction number | Reactions | Reaction constant ($M^{-1}$ $s^{-1}$ or $s^{-1}$) | Reference |
|---|---|---|---|
| 74 | $OH^{\bullet} + Cl^{-} \rightarrow ClOH^{\bullet-}$ | $4.3\times10^{9}$ | 57 |
| 75 | $ClOH^{\bullet-} \rightarrow OH^{\bullet} + Cl^{-}$ | $6.1\times10^{9}$ | 57 |
| 76 | $Cl^{\bullet} + Cl^{-} \rightarrow Cl_2^{\bullet-}$ | $8.5\times10^{9}$ | 57 |
| 77 | $H^{+} + ClOH^{\bullet-} \rightarrow Cl^{\bullet} + H_2O$ | $2.1\times10^{10}$ | 57 |
| 78 | $ClOH^{\bullet-} \rightarrow Cl^{\bullet} + OH^{-}$ | $2.3\times10^{1}$ | 57 |
| 79 | $Cl^{\bullet} + OH^{-} \rightarrow ClOH^{\bullet-}$ | $1.8\times10^{10}$ | 57 |
| 80 | $Cl_2^{\bullet-} \rightarrow Cl^{\bullet} + Cl^{-}$ | $6.0\times10^{4}$ | 57 |
| 81 | $Cl_2^{\bullet-} + Cl_2^{\bullet-} \rightarrow Cl_3^{-} + Cl^{-}$ | $2.0\times10^{9}$ | 57 |
| 82 | $Cl^{\bullet} + Cl_2^{\bullet-} \rightarrow Cl_3^{-}$ | $6.3\times10^{8}$ | 57 |
| 83 | $Cl^{-} + Cl_2 \rightarrow Cl_3^{-}$ | $1.0\times10^{4}$ | 57 |
| 84 | $Cl_3^{-} \rightarrow Cl^{-} + Cl_2$ | $5.0\times10^{4}$ | 57 |
| 85 | $Cl^{\bullet} + Cl^{\bullet} \rightarrow Cl_2$ | $8.8\times10^{7}$ | 57 |
| 86 | $e_{aq}^{-} + Cl^{\bullet} \rightarrow Cl^{-}$ | $1.0\times10^{10}$ | 57 |
| 87 | $e_{aq}^{-} + Cl_2^{\bullet-} \rightarrow 2Cl^{-}$ | $1.0\times10^{10}$ | 57 |
| 88 | $e_{aq}^{-} + Cl_3^{-} \rightarrow Cl^{-} + Cl_2^{\bullet-}$ | $3.0\times10^{10}$ | 57 |
| 89 | $H^{\bullet} + Cl^{\bullet} \rightarrow H^{+} + Cl^{-}$ | $1.0\times10^{10}$ | 57 |
| 90 | $H^{\bullet} + Cl_2^{\bullet-} \rightarrow H^{+} + 2Cl^{-}$ | $8.0\times10^{9}$ | 57 |
| 91 | $H^{\bullet} + Cl_3^{-} \rightarrow H^{+} + Cl^{-} + Cl_2^{\bullet-}$ | $1.0\times10^{10}$ | 57 |
| 92 | $HO_2^{\bullet} + Cl_2^{\bullet-} \rightarrow 2Cl^{-} + O_2 + H^{+}$ | $1.0\times10^{9}$ | 57 |
| 93 | $HO_2^{\bullet} + Cl_2 \rightarrow Cl_2^{\bullet-} + O_2 + H^{+}$ | $1.0\times10^{9}$ | 58 |
| 94 | $HO^{\bullet} + HSO_4^{-} \rightarrow H_2O + SO_4^{-}$ | $4.7\times10^{5}$ | 59 |
| 95 | $H^{\bullet} + S_2O_8^{2-} \rightarrow SO_4^{-} + HSO_4^{-}$ | $2.5\times10^{7}$ | 59 |
| 96 | $H^{\bullet} + HSO_5^{-} \rightarrow H_2O + SO_4^{-}$ | $2.2\times10^{8}$ | 59 |
| 97 | $H^{\bullet} + SO_4^{-} \rightarrow HSO_4^{-}$ | $1.0\times10^{10}$ | 59 |
| 98 | $SO_4^{-} + SO_4^{-} \rightarrow S_2O_8^{2-}$ | $7.6\times10^{8}$ | 59 |
| 99 | $SO_4^{-} + H_2O_2 \rightarrow HSO_4^{-} + HO_2$ | $1.2\times10^{7}$ | 59 |
| 100 | $SO_4^{-} + HO_2 \rightarrow HSO_4^{-} + O_2$ | $3.5\times10^{9}$ | 59 |
| 101 | $SO_4^{-} + HO^{\bullet} \rightarrow HSO_5^{-}$ | $1.0\times10^{9}$ | 59 |
| 102 | $SO_4^{-} + H_2O \rightarrow HSO_4^{-} + HO^{\bullet}$ | $500\ s^{-1}$ | 59 |
| 103 | $Tris + HO^{\bullet} \rightarrow Tris^{\bullet} + H_2O$ | $3.4\times10^{8}$ | This Work |
| 104 | $TrisH^{+} + HO^{\bullet} \rightarrow Tris^{\bullet+} + H_2O$ | $9.8\times10^{8}$ | This Work |
| 105 | $Tris + H^{+} \rightarrow TrisH^{+}$ | $1.0\times10^{10}$ | $pK_a = 8.08$ |
| 106 | $TrisH^{+} \rightarrow Tris + H^{+}$ | $83.2\ s^{-1}$ | $pK_a = 8.08$ |
| 107 | $Tris^{\bullet} + H^{\bullet} \rightarrow Tris$ | $1.0\times10^{9}$ | Estimate |
| 108 | $Tris^{\bullet+} + H^{\bullet} \rightarrow TrisH^{+}$ | $1.0\times10^{9}$ | Estimate |
| 109 | $SO_4^{2-} + H^{+} \rightarrow HSO_4^{-}$ | $1.0\times10^{10}$ | $pK_a = 1.92$ |
| 110 | $HSO_4^{-} \rightarrow SO_4^{2-} + H^{+}$ | $1.2\times10^{8}\ s^{-1}$ | $pK_a = 1.92$ |

**Table S3.** Summary of reactions included in the chemical kinetics model network (*57–59*).

| Simulation No. | Corresponding panels | Electron fluence rate | $[TrisH^{+}]$ (mM) | $[Cl^{-}]$ (mM) | $[SO_4^{2-}]$ (mM) | pH |
|---|---|---|---|---|---|---|

| | | $(e^{-}\cdot Å^{-2}\cdot s^{-1})$ | | | | |
|---|---|---|---|---|---|---|
| 1 | Fig. S5A and S6A | 400 | 10 | 10 | 0 | 5.0 |
| 2 | Fig. S5B and S6B | 400 | 10 | 0 | 5.0 | 5.0 |
| 3 | Fig. S5C and S6C | 2000 | 10 | 10 | 0 | 5.0 |
| 4 | Fig. S5D and S6D | 2000 | 10 | 0 | 5.0 | 5.0 |

**Table S4.** Summary of the fluence rates and initial concentrations used for modeling the chemical reaction networks under electron radiolysis.

| Movie ID | Corresponding figures | Solution used for encapsulation | Electron fluence rate ($e^{-}$·Å$^{-2}$·s$^{-1}$) | Acquisition frame rate (frame per second) |
|---|---|---|---|---|
| S1 | Fig. 2 and Fig. S9-S10 | 10 mM Tris•HCl | 400 | 4 |
| S2 | Fig. 2 and Fig. S11 | 10 mM Tris•HCl | 2000 | 8 (left panel); 6 (right panel) |
| S3 | Fig. 3 and Fig. S23 | 10 mM Tris•HCl | 400 | 4 |
| S4 | Fig. 3 and Fig. S24 | 10 mM Tris•HCl | 2000 | 10 (left panel); 15 (right panel) |
| S5 | Fig. S27 | 10 mM Tris•HCl | 800 | 4 |
| S6 | Fig. S28 | 10 mM Tris•HCl | 2000 | 10 |
| S7 | Fig. 4 and Fig. S30 | 10 mM Tris•HCl | 400 | 4 |
| S8 | Fig. S1 | 10 mM Tris•0.5$H_2SO_4$ | 400 | 4 |

**Table S5.** Summary of the experimental parameters and contents of LCTEM movies collected for this study.

**Movie S1.** The etching of two individual PbSe nanocrystals recorded at 400 $e^{-}\cdot Å^{-2}\cdot s^{-1}$. The replicas were recorded independently during two LCTEM experiments. The contents of the liquid pockets were water and Tris•HCl.

**Movie S2.** The rapid etching of two individual PbSe nanocrystals recorded at 2000 $e^{-}\cdot Å^{-2}\cdot s^{-1}$. The replicas were recorded independently during two LCTEM experiments. The contents of the liquid pockets were water and Tris•HCl.

**Movie S3.** The etching of two individual $\{\acute{1}\,100\}$-terminated CdSe nanocrystals recorded at 400 $e^{-}\cdot Å^{-2}\cdot s^{-1}$. The replicas were recorded independently during two LCTEM experiments. The contents of the liquid pockets were water and Tris•HCl.

**Movie S4.** The rapid etching of two individual $\{\acute{1}\,100\}$-terminated CdSe nanocrystals recorded at 2000 $e^{-}\cdot Å^{-2}\cdot s^{-1}$. The replicas were recorded independently during two LCTEM experiments. The contents of the liquid pockets were water and Tris•HCl.

**Movie S5.** The etching of two individual $\{11\acute{2}\,0\}$-terminated CdSe nanocrystals recorded at 800 $e^{-}\cdot Å^{-2}\cdot s^{-1}$. The replicas were recorded independently during two LCTEM experiments. The contents of the liquid pockets were water and Tris•HCl.

**Movie S6.** The rapid etching of two individual $\{11\acute{2}\,0\}$-terminated CdSe nanocrystals recorded at 2000 $e^{-}\cdot Å^{-2}\cdot s^{-1}$. The replicas were recorded independently during two LCTEM experiments. The contents of the liquid pockets were water and Tris•HCl.

**Movie S7.** The etching of two individual CdSe nanocrystals with low aspect ratio viewed along the *c*-axis. The prismatic facets are $\{\acute{1}\,100\}$-terminated. The movies were recorded at 400 $e^{-}\cdot Å^{-2}\cdot s^{-1}$. The replicas were recorded independently during two LCTEM experiments. The contents of the liquid pockets were water and Tris•HCl.

**Movie S8.** The movie shows that the etching of PbSe nanocrystals was observed when the contents of the liquid pockets were water and Tris•$0.5H_2SO_4$. The two replicas were recorded at 400 $e^{-}\cdot Å^{-2}\cdot s^{-1}$ independently during two LCTEM experiments.